

Statistical state dynamics based study of turbulent Eady fronts. Part 2. Finite amplitude equilibria

Eojin Kim^{†1}, Brian F. Farrell¹

¹Department of Earth and Planetary Sciences, Harvard University, Cambridge, MA 02138, USA

(Received 18 Dec. 2015; revised 29 Sep. 2016; accepted 9 Oct. 2016)

Streamwise roll circulations commonly observed in frontal regions are primary agents of momentum and tracer transport in the planetary boundary layer (PBL) both in the atmosphere and ocean. Traditionally, the formation of the streamwise roll/streak structure (RSS) has been ascribed to symmetric instability (SI). In part 1, we studied RSS formation in the classical Eady front problem using statistical state dynamics (SSD), which allows incorporating the Reynolds stress (RS) torque instability mechanism together with SI in the dynamics underlying RSS formation. We found using SSD theory that the RS torque mechanism acts synergistically with the SI mechanism in forcing symmetric circulations in fronts when Richardson number $Ri < 1$, and also that the turbulence-mediated RS torque mechanism supports RSS formation in fronts with $Ri > 1$ for which the SI mechanism does not operate. Although SI theory provides an explanation for initial roll formation, it leaves open the question of RSS equilibration. An advantage of the SSD formulation of RSS dynamics is that it consistently incorporates the equilibration process. In this paper, we extend perturbation analysis of RSS dynamics in the SSD framework to a nonlinear analysis to understand roll formation, equilibration, and maintenance in the turbulent RSS regime.

Key words: PBL, mixed layer, statistical state dynamics, front

1. Introduction

Fronts are narrow zones of intensified horizontal velocity and buoyancy gradients that emerge prominently within the stratified planetary boundary layer (PBL) as regions in near thermal wind balance between streamwise velocity and buoyancy fields. In the upper ocean mixed layer (spanning 10-100 m depths), fronts form concentrated regions of air-sea exchange that are responsible for a substantial component of the vertical transport of heat, momentum, and tracers. These transports are produced by both large-scale coherent structures and small-scale turbulence, with the coherent roll-streak structure (RSS) responsible for a substantial component.

Although simplified, the Eady model that we employ in this study has proved to be a powerful tool for investigating the dynamics of fronts in rotating stratified flows. By simulating a vertically sheared zonal flow in thermal wind balance with a constant lateral temperature gradients, this model allows investigation of how buoyancy forces and Reynolds stress (RS) torque interact to generate coherent RSS. In part 1 (Kim & Farrell 2025), we formulated an SSD theory for the Eady front model. Expressing the Navier-Stokes equations in SSD form enabled us to analytically investigate the synergy

[†] Email address for correspondence: ekim@g.harvard.edu

between the symmetric instability (SI) and the RS torque instability in RSS formation. We found that the RS torque mechanism acts synergistically with the SI instability in frontal regions where $R_i < 1$ and continues to support the RSS instability where $R_i > 1$, a region of parameter space for which SI is not supported. In a manner similar to roll structures arising from SI, rolls destabilized by the RS torque mechanism produce parcel trajectories close to isopycnal surfaces over the interior of the domain that cross isopycnals to close near the upper and lower boundaries. The interior coincidence of trajectories of parcels and isopycnal surfaces is consistent with the structure of transient optimals supported by the Eady front model (Zemskova *et al.* 2019). Notably, these authors found transient optimals to exhibit symmetric circulations coincident with isopycnal surfaces regardless of Richardson number, Ri . Although both SI and the RS torque mechanism instability support similar RSS structures, the dynamics underlying these roll formation instabilities differs. The SI RSS arises primarily from buoyancy forcing while the RS torque mechanism RSS arises primarily from fluctuation Reynolds stress forcing. Despite differences in their RSS dynamics, we found in part 1 that the SI and RS torque mechanism instabilities act synergistically in creating roll circulations.

The S3T SSD for the Eady front model developed for studying RSS perturbation stability in part 1 contains the nonlinear dynamics producing equilibration of those instabilities at finite amplitude, which is the subject of part 2. Observational data suggest that the RSS exploits both the SI mechanism and the turbulence-mediated RS torque mechanism to establish nonlinear equilibrium states. For example, (Zhou *et al.* 2022) reports turbulent mixing in the thermocline at low latitude, especially in the convergence regions of the north-equatorial countercurrent. Although high turbulent mixing is observed, their figure 3 reveals that most of the domain is characterized by positive potential vorticity and/or Richardson number greater than unity, implying stability to SI. Although the authors point to limited regions with negative or zero potential vorticity to suggest that mixing could be driven by SI-generated rolls, their observations show that energy production associated with SI is significantly less than turbulence dissipation, except in narrowly restricted regions, implying that their observed RSS states are being supported by mechanisms other than SI. Their data also reveal subduction of phytoplankton below the mixed layer to depths of a kilometer, as well as subduction of cold, fresh, and oxygenated water patches below unstable fronts to intermediate depths of $200m - 600m$, while observational data show limited regions of negative potential vorticity that could support symmetric instability, while most of the mixed region is stable to symmetric instability. Taken as a whole, disparities between conditions for SI and observations of RSS states motivate the search for alternative roll-forming /vertical mixing mechanisms in frontal regions.

When acting alone, SI does not appear to be associated with a straightforward equilibration process. Simulations have been interpreted to suggest an equilibration sequence proceeding from the growth of SI leading to the development of shears within rolls leading to Kelvin Helmholtz instability, then to PV adjustment, which eventually leads to inertial oscillations (Stamper & Taylor 2016; Taylor & Ferrari 2009). Unlike this sequential equilibration process, our results from nonlinear SSD simulation of the Eady front suggest a relatively simple equilibration process in which over the interior frontal region the SI instability is suppressed by increasing stratification while the RS torque mechanism maintains the RSS equilibrium state at $R_i > 1$. We find fixed-point, time-dependent, and turbulent equilibria for RSS regimes across our parameter space.

2. Formulation of the SSD for the Eady front model

The focus of part 1 was on developing the S3T SSD theory for the study of instabilities of turbulent equilibria of the Eady front, the focus of this paper is on non-linear turbulent equilibria proceeding from these instabilities. To this end, we apply the Eady model SSD; which we first used in part 1 to study perturbation SSD dynamics, to the study of finite amplitude SSD solutions.

Our coordinate system is streamwise direction x , wall normal direction y , and vertical direction z ; velocity components are u , v , and w , with associated unit vectors \mathbf{i} , \mathbf{j} , \mathbf{k} , respectively.

In the Eady model equilibrium state both the vertical shear of the zonal velocity and the spanwise buoyancy gradient are constant. Thermal wind balance between the equilibrium state zonal velocity, $U_G(y)$, and buoyancy, b_G , requires:

$$\frac{dU_G(y)}{dy} = \frac{1}{f} \frac{db_G}{dz}. \quad (2.1)$$

The total velocity and total buoyancy can be decomposed into the equilibrium state and perturbations as:

$$\underline{u}_T = U_G(y)\mathbf{i} + \underline{u}(x, y, z, t) \quad (2.2)$$

$$b_T = b_G(z) + b(x, y, z, t) \quad (2.3)$$

where $U_G(y)$ and $b_G(z)$ are the Eady equilibrium velocity and buoyancy components consistent with thermal wind balance. In the Eady model equilibrium state these are written as:

$$b_G(z) = M^2 z \quad (2.4)$$

$$U_G(y) = \frac{M^2}{f} y \quad (2.5)$$

In which M^2 is the spanwise Eady equilibrium buoyancy gradient. The corresponding equilibrium velocity \underline{u}_{Te} and buoyancy b_{Te} are:

$$b_{Te} = N^2 y + M^2 z \quad (2.6)$$

$$\underline{u}_{Te} = U_G(y)\mathbf{i} \quad (2.7)$$

where N^2 is the vertical buoyancy gradient.

The governing equations for \underline{u} and b are:

$$\frac{\partial \underline{u}}{\partial t} + (\underline{u}_T \cdot \nabla) \underline{u}_T = -\nabla \Pi - f \mathbf{j} \times \underline{u} + \nu \Delta \underline{u} + b \mathbf{j} \quad (2.8)$$

$$\frac{\partial b}{\partial t} + (\underline{u}_T \cdot \nabla)b + wM^2 = \kappa \Delta b \quad (2.9)$$

where $\Delta := (\partial_{xx} + \partial_{yy} + \partial_{zz})$. With the exception of taking x as the streamwise direction, y as the vertical (wall normal) direction, and z as the spanwise direction, this equation is as in (Taylor & Ferrari 2010).

Velocity is non-dimensionalized by $M^2 H/f$; with the vertical length scale, H , taken to be the height of the upper boundary; this velocity scale corresponds to the shear across the domain in the vertical direction. Consistently, time is nondimensionalized by f/M^2 . Nondimensional parameters are:

$$\Gamma = \frac{M^2}{f^2}, Re = \frac{H^2 M^2}{f\nu}, Ri = \frac{N^2 f^2}{M^4}, Pr = \frac{\nu}{\kappa} \quad (2.10)$$

corresponding to the Rossby, Reynolds, Richardson and Prandtl numbers respectively.

Nondimensional equilibrium velocity and buoyancy are:

$$b_{Te} = y + \frac{1}{Ri \cdot \Gamma} z \quad (2.11)$$

$$\underline{u}_{Te} = y \mathbf{i} \quad (2.12)$$

Nondimensionalized equations are

$$\frac{\partial \underline{u}}{\partial t} + (\underline{u}_T \cdot \nabla) \underline{u}_T = -\nabla \Pi - \frac{1}{\Gamma} \mathbf{j} \times \underline{u} + \frac{1}{Re} \Delta \underline{u} + Ri \cdot \mathbf{b} \mathbf{j} \quad (2.13a)$$

$$\frac{\partial b}{\partial t} + (\underline{u}_T \cdot \nabla)b + w \frac{1}{Ri \cdot \Gamma} = \frac{1}{Re Pr} \Delta b \quad (2.13b)$$

Our numerical simulation assumes periodic boundary conditions in both the streamwise direction, x , and the spanwise direction, z . In the wall-normal direction, y , stress free and zero buoyancy flux conditions are applied at both the top and bottom. Other studies have used stress and buoyancy boundary fluxes to destabilize the symmetric instability (Taylor & Ferrari 2010; Haine & Marshall 1997). Our boundary conditions precluded this mechanism.

3. SSD Formulation

Formulation of the SSD equations requires decomposing variables into mean and fluctuation components. The means we use are \overline{A} , indicating a Reynolds average of quantity A , and $[A]_x$, indicating quantity A averaged in the x direction. Velocity, \underline{u} , and buoyancy, b , decomposed into mean and fluctuations are:

$$\underline{u}(x, y, z, t) = \underline{U}(y, z, t) + \underline{u}'(x, y, z, t) \quad (3.1)$$

$$b(x, y, z, t) = B(y, z, t) + b'(x, y, z, t) \quad (3.2)$$

taking capital letters to denote a Reynolds averaged variable, we indicate our choice of

the streamwise average for our Reynolds average so that:

$$\bar{u} = [\underline{u}]_x = U \quad (3.3)$$

$$\bar{b} = [\underline{b}]_x = B \quad (3.4)$$

Our choice of the streamwise average for our Reynolds average anticipates that the RSS instability will break the symmetry of our model in the spanwise direction and that the resulting RSS, whether the initial unstable mode or the equilibrium state, can be conveniently isolated in the first cumulant by not including the spanwise mean in the Reynolds average when formulating our SSD. Equations for mean velocity \underline{U} and mean buoyancy B can be obtained by taking the streamwise mean of equation 2.13

$$U_t = (U_y + 1)\Psi_z - U_z\Psi_y - \partial_y \overline{u'v'} - \partial_z \overline{u'w'} + \Delta_1 \frac{U}{Re} - \frac{\Psi_y}{\Gamma} \quad (3.5a)$$

$$\Delta_1 \Psi_t = (\partial_{yy} - \partial_{zz})(\Psi_y \Psi_z - \overline{v'w'}) - \partial_{yz}(\Psi_y^2 - \Psi_z^2 + \overline{w'^2} - \overline{v'^2}) + \Delta_1 \Delta_1 \frac{\Psi}{Re} - Ri \cdot \frac{\partial B}{\partial z} + \frac{1}{\Gamma} \frac{\partial U}{\partial y} \quad (3.5b)$$

$$B_t = -\left(\frac{1}{Ri \cdot \Gamma} + B_z\right)\Psi_y + B_y \Psi_z - \partial_y(\overline{b'v'}) - \partial_z(\overline{b'w'}) + \frac{1}{RePr} \Delta_1 B \quad (3.5c)$$

in which $\Delta_1 := (\partial_{yy} + \partial_{zz})$ and where we have taken advantage of nondivergence in the spanwise/cross-stream plane to write the spanwise and cross-stream velocities in streamfunction form as $W = \frac{\partial \Psi}{\partial y}$ and $V = -\frac{\partial \Psi}{\partial z}$. Expressing our streamwise mean solution velocity component in terms of U and Ψ indicates isolation of the RSS structures into the first cumulant.

Equations for the fluctuation components of velocity \underline{u}' and buoyancy b' are obtained by subtracting mean equations 3.5 from equations 2.13. The fluctuation velocity dynamics is expressed in the wall normal velocity and wall normal vorticity formulation by which nondivergence of velocity is intrinsically incorporated (Schmid & Henningson 2001).

Fluctuation velocity, vorticity and buoyancy are decomposed into streamwise wavenumber components as

$$v'(x, y, z, t) = \sum_k v'_k(y, z, t) e^{ikx} \quad (3.6)$$

$$\eta'(x, y, z, t) = \sum_k \eta'_k(y, z, t) e^{ikx} \quad (3.7)$$

$$b'(x, y, z, t) = \sum_k b'_k(y, z, t) e^{ikx} \quad (3.8)$$

We can now incorporate the fluctuation velocity equations in the wall normal velocity-vorticity formulation into our perturbation equations to obtain these equations in the compact form:

$$\frac{\partial \hat{\phi}_k}{\partial t} = A \hat{\phi}_k + \xi_k \quad (3.9)$$

in which the fluctuation state vector is:

$$\hat{\phi}_k = \begin{bmatrix} v'_k \\ \eta'_k \\ b'_k \end{bmatrix} \quad (3.10)$$

and we have parameterized the fluctuation-fluctuation nonlinear term by a stochastic noise process $\xi(t)$. We note that in applying this model to physical problems, this stochastic noise process incorporates also any external sources of turbulent fluctuations.

The matrix of the dynamics is:

$$A = \begin{bmatrix} A_{11} & A_{12} & A_{13} \\ A_{21} & A_{22} & A_{23} \\ A_{31} & A_{32} & A_{33} \end{bmatrix} \quad (3.11)$$

$$A_{11} = L_{OS}(U + U_G) + \Delta^{-1}(LV_{11}(V) + LW_{11}(W)) \quad (3.12)$$

$$A_{12} = L_{C1}(U + U_G) + \Delta^{-1}(LV_{12}(V) + LW_{12}(W)) - \Delta^{-1}\left(\frac{1}{\Gamma}\partial_y\right) \quad (3.13)$$

$$A_{13} = Ri\Delta^{-1}\Delta_2 \quad (3.14)$$

$$A_{21} = L_{C2}(U + U_G) + LV_{21}(V) + LW_{21}(W) + \frac{1}{\Gamma}\partial_y \quad (3.15)$$

$$A_{22} = L_{SQ}(U + U_G) + Lv_{22}(V) + LW_{22}(W) \quad (3.16)$$

$$A_{23} = 0 \quad (3.17)$$

$$A_{31} = -\partial_y(B + b_G) + \partial_z(B + b_G)\Delta_2^{-1}\partial_{yz} \quad (3.18)$$

$$A_{32} = \partial_z(B + b_G)\Delta_2^{-1}(ik) \quad (3.19)$$

$$A_{33} = -(U + U_G)(ik) + \Psi_z\partial_y - \Psi_y\partial_z + \frac{1}{RePr}\Delta \quad (3.20)$$

where $\Delta_2 := (\partial_{xx} + \partial_{zz})$.

$L_{OS}(U + U_G)$ is the Orr Sommerfeld operator with $U + U_G$ the streamwise mean velocity. For details on the Orr-Sommerfeld-Squire form of the dynamics see (Farrell & Ioannou 2012). Details of component equations 3.12 – 3.16 are provided in the appendix. Following the SSD formulation as outlined in (Farrell & Ioannou 2019), a deterministic Lyapunov equation can be obtained for the ensemble average fluctuation covariance, C , solely from knowledge of A and the assumption of a white in time noise process with spatial covariance $\epsilon Q := \langle \xi \xi^\dagger \rangle$:

$$\frac{dC_k}{dt} = AC_k + C_kA^\dagger + \epsilon Q \quad (3.21)$$

$$C_k = \hat{\phi}_k \hat{\phi}_k^\dagger \quad (3.22)$$

where † denotes the Hermitian transpose and a scalar parameter ϵ has been included for convenience in varying the intensity of the stochastic excitation. We note that it is the remarkable existence of this time-dependent Lyapunov equation, which is equivalent to calculating the covariance (second cumulant) using an infinite ensemble of fluctuation fields sharing the single time-dependent mean state (first cumulant), that allows us to obtain the SSD in a deterministic analytic form. Turning now to the equations for the mean, we note that the Reynolds stress terms appearing in the mean equations (3.5) – (3.7) can be obtained by a linear operator, L_{RS} , applied to the covariances C_k , of the fluctuations cf. (Farrell & Ioannou 2012). Taking account of this, the equations for the mean state can be expressed in compact notation as follows:

$$\Xi_t = G(\Xi) + \sum_k L_{RS} C_k \quad (3.23)$$

where $\Xi = [U, \Psi, B]^T$. In equation (3.25), G is:

$$G(\Xi) = \left[\begin{array}{c} (U_y + 1)\Psi_z - U_z\Psi_y + \Delta_1 \frac{U}{Re} - \frac{\Psi_y}{\Gamma} \\ \Delta_1^{-1} [(\partial_{yy} - \partial_{zz})(\Psi_y\Psi_z) - \partial_{yz}(\Psi_y^2 - \Psi_z^2) + \Delta_1 \Delta_1 \frac{\Psi}{Re} - Ri \cdot \frac{\partial B}{\partial z} + \frac{1}{\Gamma} \frac{\partial U}{\partial y}] \\ -(\frac{1}{Ri \cdot \Gamma} + B_z)\Psi_y + B_y\Psi_z + \frac{1}{RePr} \Delta_1 B \end{array} \right] \quad (3.24)$$

and the forcing by the fluctuation stresses at each k is:

$$L_{RS} C_k = \left[\begin{array}{c} -\partial_y \overline{u'v'}|_k - \partial_z \overline{u'w'}|_k \\ \Delta_1^{-1} [(\partial_{yy} - \partial_{zz})(-\overline{v'w'}|_k) - \partial_{yz}(\overline{w'^2}|_k - \overline{v'^2}|_k)] \\ -\partial_y (\overline{b'v'}|_k) - \partial_z (\overline{b'w'}|_k) \end{array} \right] \quad (3.25)$$

in which the fluctuation stress operator L_{RS} has been composed using these linear operators:

$$\begin{aligned} L_{u'}^k &= [-ik\Delta_2^{-1}\partial_y, \Delta_2^{-1}\partial_z, 0] \\ L_{v'}^k &= [I, 0, 0] \\ L_{w'}^k &= [-\Delta_2^{-1}\partial_{yz}, -ik\Delta_2^{-1}, 0] \\ L_{b'}^k &= [0, 0, I]. \end{aligned} \quad (3.26)$$

For instance, when a grid based method is used in both y and z:

$$\overline{u'v'}|_k = \text{diag}(L_{u'}^k C_k L_{v'}^{k\dagger}) \quad (3.27)$$

The other stress terms are written in a similar way. Note that stress terms $\sum_k L_{RS} C_k$

are linear in C_k .

We use for our RSS stability analysis an SSD closed at second order, the formulation of which is referred to as S3T. This SSD consists of the first and second cumulant together with a stochastic closure. The S3T equations can be written compactly as:

$$\Xi_t = G(\Xi) + \sum_k L_{RS} C_k \quad (3.28)$$

$$\frac{dC_k}{dt} = AC_k + C_k A^\dagger + \epsilon Q.$$

The spatial covariance of the stochastic closure, Q , is chosen to excite each degree of freedom with unit kinetic energy. It follows that buoyancy fluctuations arise from velocity fluctuations but are not directly excited. White in kinetic energy excitation is accomplished by choosing Q as follows (Farrell & Ioannou 2012):

$$Q = M_k^{-1} \quad (3.29)$$

$$M_k = (L_{u'}^{k\dagger} L_{u'}^k + L_{v'}^{k\dagger} L_{v'}^k + L_{w'}^{k\dagger} L_{w'}^k) / (2 * Ny * Nz) \quad (3.30)$$

This completes the formulation of the SSD.

4. Formulation of the S3T SSD for the Eady front model

In part 1, we used linear perturbation analysis of the S3T SSD to study the initial roll formation process in the Eady front model. In this paper, our focus turns to the equilibration of these instabilities in the nonlinear S3T SSD.

Our boundary conditions in y are insulating and stress-free. While boundary fluxes of momentum and buoyancy can destabilize the SI, resulting in what is referred to as forced symmetric instability (FSI) (Haine & Marshall 1997), and this could explain vertical mixing in near-surface frontal regions; alternative mechanisms are required to explain observations such as mixing of sea surface tracers down to 600 meters while surface flux-related FSI is unable to sustain circulations much below 50 meter depth as boundary fluxes affect PV and Richardson number primarily to this depth (Thomas 2005).

By contrast, as shown in part 1, while RSS arising from the RS torque mechanism exhibits structural similarity to RSS arising from SI, the RS torque mechanism destabilizes symmetric circulation through cooperative interaction between the RSS and the field of background turbulence and is independent of SI (Nikolaidis *et al.* 2024). The RS torque mechanism for forming and maintaining the RSS does not have an intrinsic scale, requires only a shear flow and a field of background turbulence, and operates over a wide range of ocean and atmospheric mixed layer conditions that do not support SI.

Consistent with the goal of understanding the formation and equilibration of RSS in the interior of the mixed layer, we confine our attention to the center of the channel $0.25 \leq y \leq 0.75$. To this end, we have employed sponge layers implemented by Rayleigh damping near both the top and bottom boundaries to minimize the effects of the boundaries

on the interior RSS dynamics and to suppress waves that arise as a result of the boundary conditions. This sponge layer has the form $r(y) = r_{sp}[1 - \tanh(\frac{y + \frac{y}{L_y/2} - 1/2}{\delta_{sp}})] + r_{sp}[1 + \tanh(\frac{y + \frac{y}{L_y/2} - 1/2}{\delta_{sp}})]$, in which r_{sp} is the Rayleigh damping parameter. The simulation fronts are relaxed back to thermal wind balance using Rayleigh damping $r_s = 0.025$, corresponding to a 10 day time scale, unless otherwise indicated. Although sufficiently strong relaxation would maintain SI, our weak relaxation rate r_s ensures that this mechanism is precluded while capturing the physics of the equilibration process.

For simplicity, we assume unit Prandtl number in our examples. Our Reynolds number is 400, which can be regarded as accounting for diffusion by the unresolved fluctuation component. The dynamically active component of the fluctuation field is explicitly simulated by the second cumulant equation. Our simulations have resolution $Nz = 21$ by $Ny = 40$ in the wall normal and spanwise directions. For convenience, Q in equation 3.28 is replaced by \tilde{Q} such that $\epsilon = 1$ results in volume averaged RMS perturbation velocity being 1% of the maximum velocity of the Eady model profile. Explicitly, $\sqrt{2} \langle E_k \rangle = 0.01$ where $\langle E_k \rangle = \text{trace}(M_k C_k)$ represents ensemble average kinetic energy density of the perturbation field as in (Farrell & Ioannou 2012).

5. Finite amplitude RSS equilibria

In part 1 we found by perturbing the Eady front model that RSS arise variously from SI, from the RS torque instability mechanism, and from these instabilities acting synergistically. In this paper, our focus is on the finite-amplitude equilibrium states that result from these instabilities. At parameter values unstable to RSS, perturbing the SSD Eady front model results in the excitation of unstable RSS eigenmodes. These instabilities may equilibrate to fixed point RSS, to time-dependent RSS, or to turbulent states, depending on the parameter regime. As a summary of our findings and to set the stage for presenting our results, an equilibrium structure diagram as a function of ϵ and Ri is shown in figure 1. We turn now to examining some dynamically salient regions of this diagram.

5.1. Fixed point RSS equilibration with initial $Ri < 1$

As revealed in figure 1, when the parameters (Ri, ϵ) are in an unstable regime, (c.f. (Kim & Farrell 2025)), fixed point RSS arise when an RSS eigenmode is slightly to moderately unstable. It is of interest to identify the structure of these fixed-point equilibria, and also to understand the physical mechanism equilibrating and maintaining them. We show below that these moderately unstable RSS eigenmodes equilibrate and are maintained at equilibrium by the mechanism of increasing gradient Richardson number Ri_g . Gradient Richardson number Ri_g is defined as

$$Ri_g = \frac{\frac{\partial B}{\partial y}}{(\frac{\partial(U+U_G)}{\partial y})^2 + (\frac{\partial W}{\partial y})^2} \quad (5.1)$$

Equilibria in the form of fixed-point and turbulent RSS states are produced by adjustment of the first cumulant (streamwise mean state) by interaction with Reynolds stresses obtained from the second cumulant (fluctuation covariance). The result of this equilibration process in the variables $[U]_z, [W]_z, [B]_z$ is shown for a simulation with initial parameters $Ri = 0.25$ and $\epsilon = 0.1$ in figure 2. At initial time $t = 0$, small random

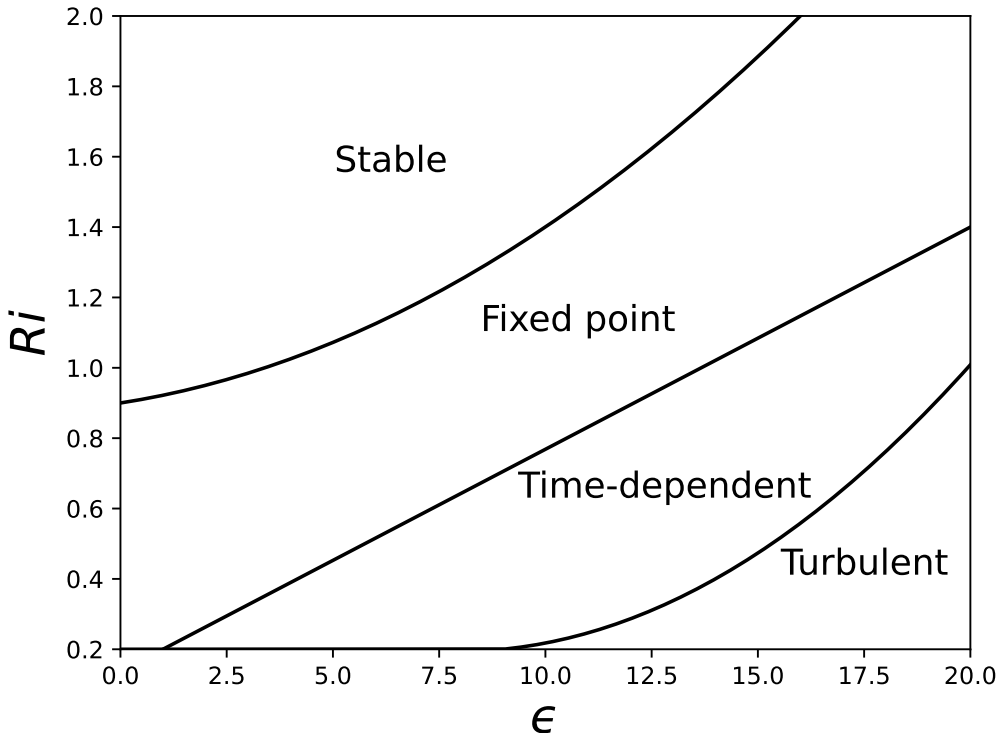


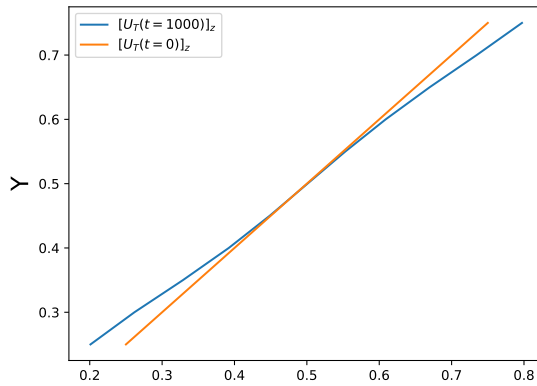
Figure 1: Equilibrium RSS state as a function of background turbulence intensity parameter, ϵ , and initial Richardson number, Ri . At sufficiently small parameter values no RSS is supported. With moderate ϵ and Ri , fixed-point RSS equilibria are supported. As these parameters increase a transition to time-dependent behavior is seen. A turbulent RSS regime emerges at high parameter values; $Re = 400$, $Pr = 1$.

perturbations were added to $\Xi, \sum_k C_k$. The equilibration is clearly the result of an increase in the Ri_g resulting primarily from an increase in the buoyancy gradient. In figure 3 the equilibrated Ri_g profile is shown and in figure 4 the associated adjustment of the RSS structure is shown during the equilibration process. Since the initial state is at $Ri = 0.25$, which makes it unstable for SI, it is consistent that the RSS observed early in the simulation are tilted toward the vertical, indicative of SI. However, as it equilibrates to its fixed-point, the RSS becomes tilted more horizontally. This is consistent with the lift-up matrix model from part 1 in which instability requires higher ϵ when Richardson number, Ri , is greater, which is also consistent with an equilibration process that proceeds by raising Ri_g until its value is that required for equilibrium with the imposed ϵ . Although the rolls observed in the earlier part of the equilibration process arise in part from SI, the equilibrated roll state has $Ri_g \approx 1.43 > 1$ making it stable to SI. We conclude that the fixed-point RSS has been equilibrated by raising Ri_g and is maintained by the RS torque mechanism at a Ri_g for which the RSS is stable to SI.

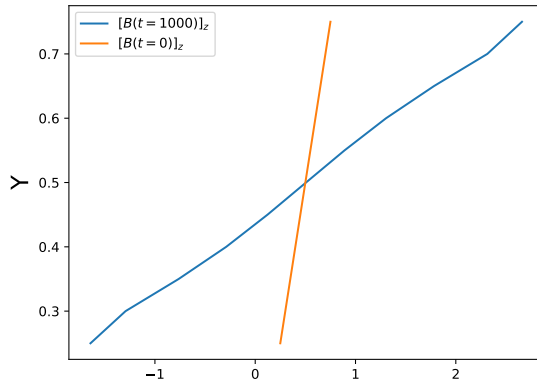
5.2. Fixed point RSS equilibration with initial $Ri > 1$

In figure 1, the regions that support fixed-point RSS are indicated. Clearly, fixed point RSS are supported even for initial $Ri > 1$. The line dividing fixed-point RSS equilibria

(a)



(b)



(c)

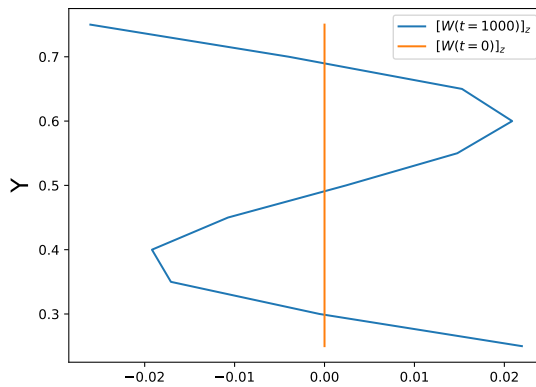


Figure 2: Equilibration of RSS mean state to fixed-point. Shown is $[U_T]_z$, $[B]_z$, and $[W]_z$ at initial time $t = 0$ and at $t = 1000$ after equilibration has taken place. Initial $Ri = 0.25$, $\epsilon = 0.1$; $Re = 400$, $Pr = 1$.

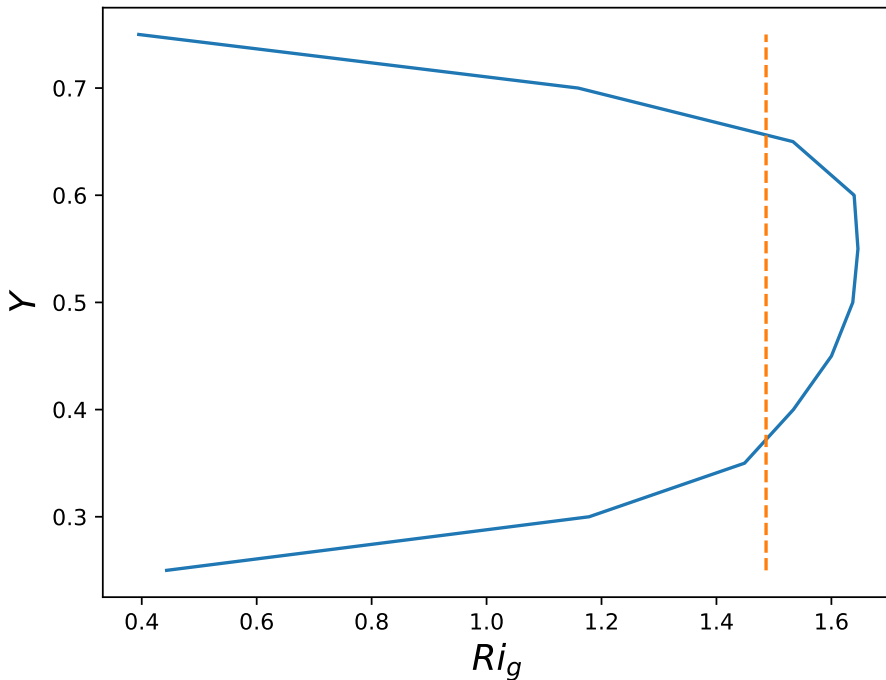


Figure 3: Gradient Richardson number $[Ri_g]_z$ of equilibrated fixed point roll solution for initial $Ri=0.25$ and with $\epsilon = 0.1$. The orange dashed line represents $[Ri_g]_z$ averaged over $0.25 \leq y \leq 0.75$; $Re = 400$, $Pr = 1$.

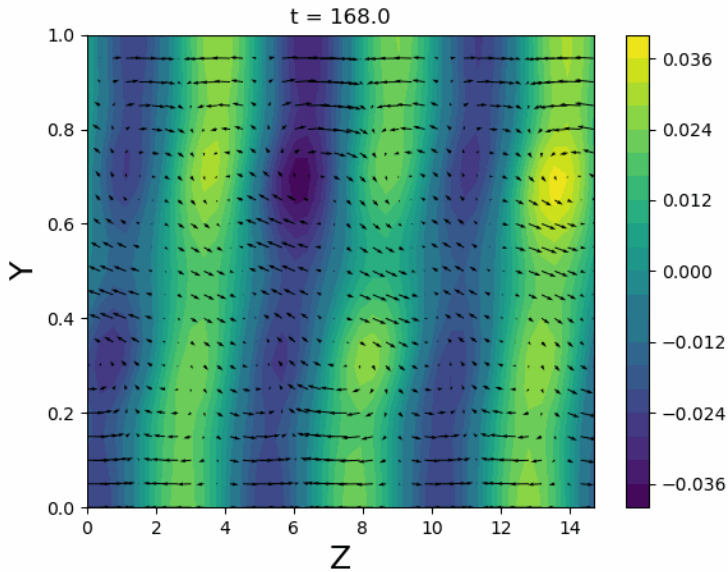
and stable regimes is consistent with lines of neutral stability from the stability diagram as a function of ϵ and Ri presented in figure 2 of part 1. The fixed-point RSS equilibrium obtained for initial $Ri = 2$ and with $\epsilon = 16$ is shown in figure 5 along with its gradient Richardson number Ri_g . At equilibrium Ri_g has average value 2.48.

While the emphasis of the last two sections has been on Ri_g and associated RSS fixed point structure, in the next section, we turn to the details of the dynamics of equilibration in the variables $[U]_z$, $[B]_z$ to provide understanding of how the RSS fixed-point is determined.

Physical mechanism maintaining $[U]_z, [W]_z, [B]_z$ in fixed-point equilibria

Fronts in the PBL are commonly observed to persist in the presence of RSS with mean background $Ri \geq 1$ and identifying the mechanism by which these fronts equilibrate is a fundamental physical problem. Although transport of momentum and buoyancy by RSS is an obvious candidate for explaining frontal equilibration, previous studies of equilibration in the Eady front model (Wienkers *et al.* 2022a,b) have been unable to identify fixed-point RSS equilibria due to development of ageostrophic flows and inertial oscillations resulting from unbalanced Coriolis forces. Including in the dynamics of $[U]_z, [W]_z, [B]_z$ the influence of both fluxes from the RSS and background turbulent Reynolds stresses

(a)



(b)

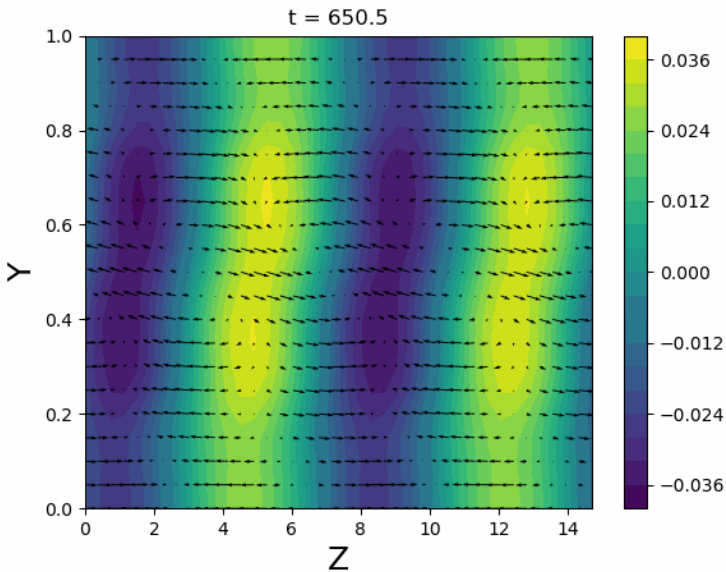
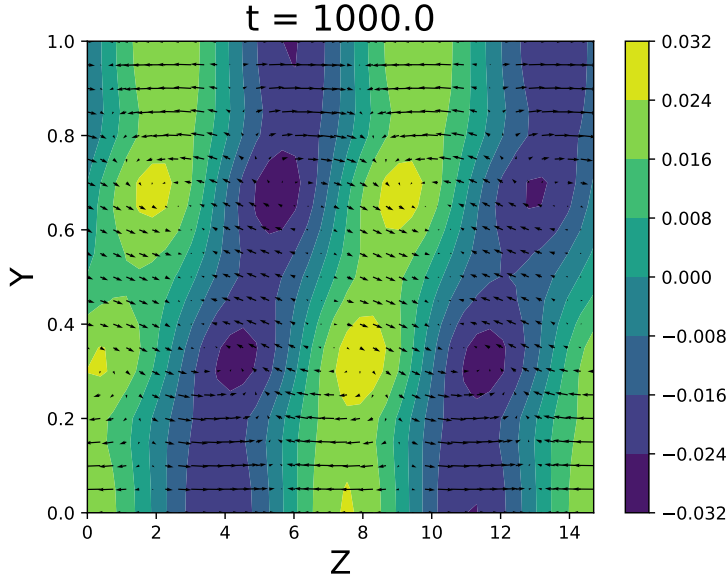


Figure 4: Equilibration of an initial $Ri = 0.25$ and $\epsilon = 0.1$ unstable RSS mode to a fixed-point roll solution. Panel (a) shows the RSS structure at the early time $t = 168$ and panel (b) shows RSS equilibrium at $t = 650.5$ at which time adjustment to equilibrium $Ri_g = 1.43$ has been obtained. These plots show that RSS structure becomes tilted more horizontally as Ri_g increases during equilibration; $\epsilon = 0.08$; $Re = 400$, $P_r = 1$.

(a)



(b)

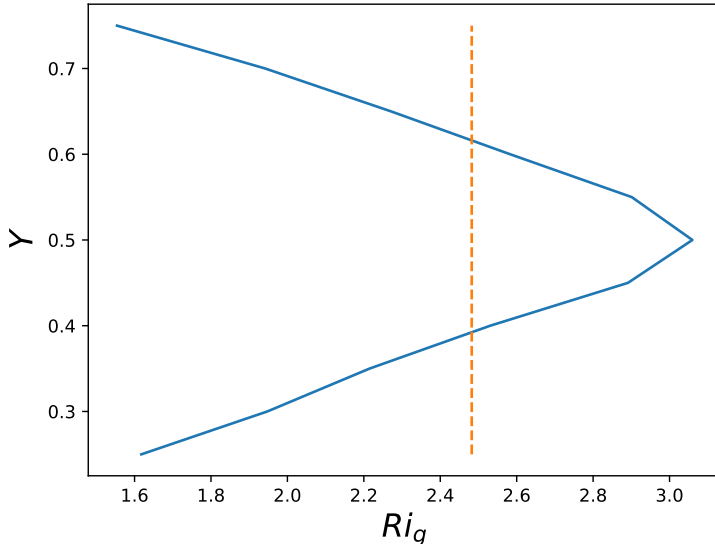


Figure 5: (a) RSS fixed-point at initial $Ri = 2$ and (b) Ri_g for this fixed-point; $\epsilon = 16$, $Re = 400$, $Pr = 1$.

using SSD demonstrates that $[U]_z, [W]_z, [B]_z$ can be maintained in steady-state dynamic balance.

In order to study the dynamics of frontal equilibration in the Eady front SSD model we begin by forming the spanwise average of the mean streamwise and spanwise velocity equations to obtain equations for $[U]_z$ and $[W]_z$:

$$\partial_t[U]_z = -\partial_y([(U+U_G)V]_z) - \partial_z([(U+U_G)W]_z) - \partial_y[u'v']_{x,z} - \partial_z[u'w']_{x,z} + \Delta_1 \frac{[U]_z}{Re} - \frac{[W]_z}{\Gamma} \quad (5.2)$$

$$\partial_t[W]_z = -\partial_y([WV]_z) - \partial_z([WW]_z) - \partial_y([w'v']_{x,z}) - \partial_z([w'w']_{x,z}) + \Delta_1 \frac{[W]_z}{Re} + \frac{[U]_z}{\Gamma}. \quad (5.3)$$

Taking account of periodic boundary condition in z allows these expressions to be further simplified to obtain:

$$\partial_t[U]_z = -\partial_y([(U+U_G)V]_z) - \partial_y[u'v']_{x,z} + \Delta_1 \frac{[U]_z}{Re} - \frac{[W]_z}{\Gamma} \quad (5.4)$$

$$\partial_t[W]_z = -\partial_y([WV]_z) - \partial_y([w'v']_{x,z}) + \Delta_1 \frac{[W]_z}{Re} + \frac{[U]_z}{\Gamma}, \quad (5.5)$$

from which the fixed-point equilibrium conditions are obtained:

$$-\partial_y([(U+U_G)V]_z) - \partial_y[u'v']_{x,z} + \Delta_1 \frac{[U]_z}{Re} - \frac{[W]_z}{\Gamma} = 0 \quad (5.6)$$

$$-\partial_y([WV]_z) - \partial_y([w'v']_{x,z}) + \Delta_1 \frac{[W]_z}{Re} + \frac{[U]_z}{\Gamma} = 0 \quad (5.7)$$

The appearance of fluctuation Reynolds stress terms in these balances suggests that the unbalanced Coriolis forces responsible for inertial oscillations may be balanced by these Reynolds stress divergences. Indeed, as seen in figure 6, $[U]_z$, $[W]_z$ are maintained in steady state by a dominant balance involving the RS flux divergence:

$$\frac{\partial[u'v']_{x,z}}{\partial y} \approx -\frac{[UV]_z}{\partial y} - \frac{[W]_z}{\Gamma} + \frac{1}{Re} \frac{\partial^2[U]_z}{\partial y^2} \quad (5.8)$$

$$\frac{\partial[w'v']_{x,z}}{\partial y} \approx -\frac{\partial[WV]_z}{\partial y} + \frac{[U]_z}{\Gamma} + \frac{1}{Re} \frac{\partial^2[W]_z}{\partial y^2} \quad (5.9)$$

Similarly, spanwise averaging of the mean buoyancy equation allows us to obtain the equation for $[B]_z$:

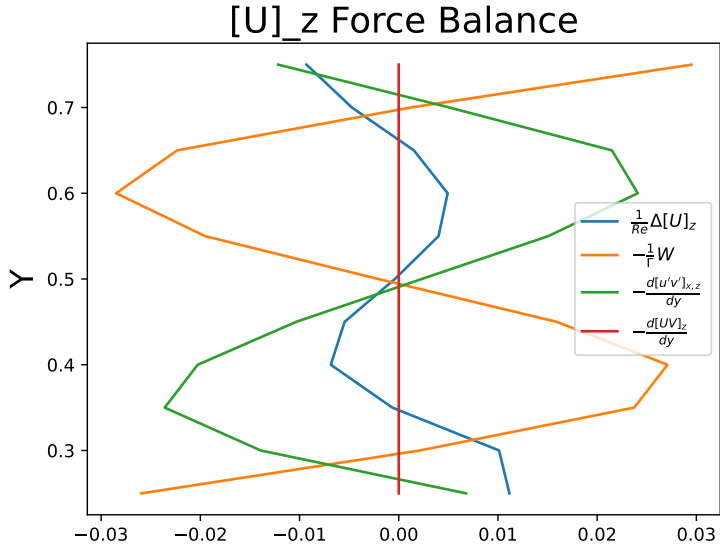
$$\partial_t[B]_z = -\frac{1}{Ri \cdot \Gamma} [W]_z - [(\partial_z B)(W)]_z - [(\partial_y B)V]_z - \partial_y([b'v']_{x,z}) - \partial_z([b'w']_{x,z}) + \frac{1}{Re \cdot Pr} \Delta[B]_z, \quad (5.10)$$

which, accounting for the periodic spanwise boundary condition, can be simplified to:

$$\partial_t[B]_z = -\frac{1}{Ri \cdot \Gamma} [W]_z - \partial_y[(B)V]_z - \partial_y([b'v']_{x,z}) + \frac{1}{Re \cdot Pr} \Delta[B]_z, \quad (5.11)$$

from which the equilibrium buoyancy balance condition for a fixed point is obtained:

(a)



(b)

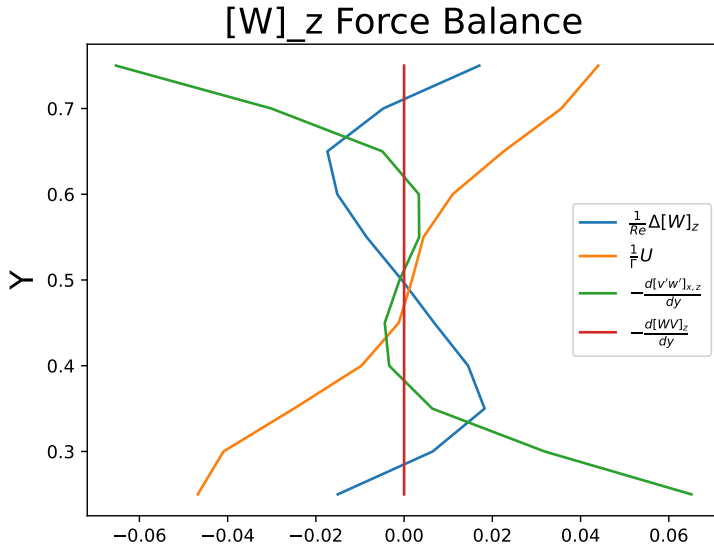


Figure 6: Contributions of the terms in the force balance maintaining the steady state fixed point mean velocity components (a) $[U]_z$ and (b) $[W]_z$; Initial $Ri = 0.25$ $\epsilon = 0.1$, $Re = 400$, $Pr = 1$.

$$-\frac{1}{Ri \cdot \Gamma} [W]_z - \partial_y [(B)V]_z - \partial_y ([b'v']_{x,z}) + \frac{1}{Re \cdot Pr} \Delta[B]_z = 0. \quad (5.12)$$

Results obtained from SSD show that the resolved fluctuation buoyancy flux divergence $-\partial_y[b'v']_{x,z}$ and the unresolved fluctuation (diffusive) buoyancy flux divergence $-\frac{1}{Re \cdot Pr} \Delta[B]_z$ co-operate to balance the spanwise buoyancy flux divergence $\frac{1}{Ri \cdot \Gamma} [W]_z$ in the interior with the resolved component playing a greater role as ϵ increases, as seen in figure 7

5.3. Mechanism maintaining streak, U_s , and roll vorticity, Ω_r , in steady state

The physical mechanism underlying RSS dynamics and equilibration can also be examined through the equations governing the RSS roll and streak components U_s and Ω_{xs} (Farrell *et al.* 2016). The equation governing the streak component in the Eady front problem can be written as:

$$\partial_t U_s = -(\partial_y(UV) - \partial_y[UV]_z) - \partial_z(UW) - (\partial_y[u'v']_x - \partial_y[u'v']_{x,z}) - \partial_z[u'w']_x + \Delta_1 \frac{U_s}{Re} - \frac{W - [W]_z}{\Gamma}, \quad (5.13)$$

where $U_S = U - [U]_z$.

Given that streaks of both signs occur, in order to obtain a linear measure of streak forcing each term is multiplied by $sign(U_s)$. The equations for the physically distinct terms in the dynamics maintaining U_S are:

$$I_A = sign(U_s) \cdot \left(-\left(V \frac{\partial U}{\partial y} - [V \frac{\partial U}{\partial y}]_z \right) - \left(W \frac{\partial U}{\partial z} - [W \frac{\partial U}{\partial z}]_z \right) \right) \quad (5.14)$$

$$I_B = sign(U_s) \cdot \left(-\left([v' \frac{\partial u'}{\partial y}]_x - [v' \frac{\partial u'}{\partial y}]_{x,z} \right) - \left([w' \frac{\partial u'}{\partial z}]_x - [w' \frac{\partial u'}{\partial z}]_{x,z} \right) \right) \quad (5.15)$$

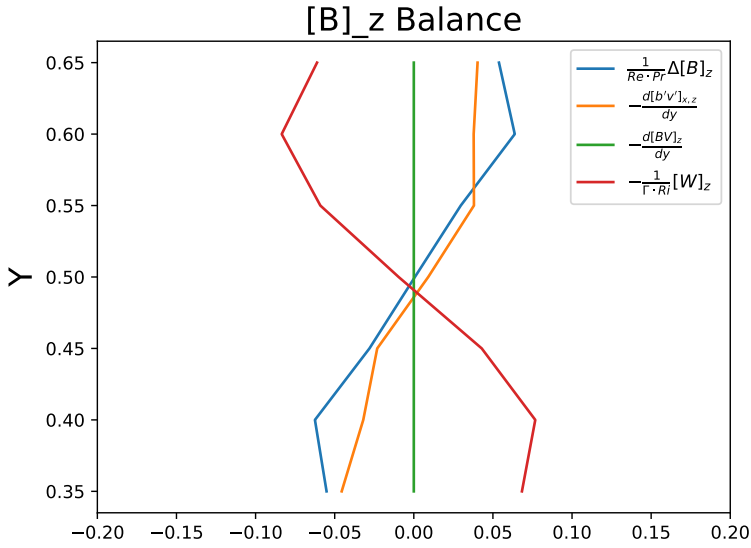
$$I_C = sign(U_s) \cdot \left(\frac{1}{Re} \Delta_1 U_s \right) \quad (5.16)$$

$$I_D = sign(U_s) \cdot \left(-\left(\frac{1}{\Gamma} W - \frac{1}{\Gamma} [W]_z \right) \right) \quad (5.17)$$

The terms I_A, I_B, I_C, I_D are the lift-up, Reynold stress divergence, diffusion, and Coriolis force, respectively. The structure of I_A, I_B, I_C, I_D for the fixed-point equilibrium RSS initiated at $Ri = 0.25$ and with $\epsilon = 0.02$ can be seen in figure 8 This figure reveals that in the absence of turbulent Reynolds stresses the streak amplitude would not be maintained as its decay rate resulting from diffusion and the Coriolis term, I_C , is significantly larger than its growth rate resulting from the lift-up mechanism, I_A . Turbulent flux divergence is required to balance the net streak decay rate resulting from dissipation, Coriolis, and lift up. Our results demonstrate that the RSS structure is unable to sustain its finite amplitude fixed point equilibrium streak in the absence of the turbulence flux term I_B .

Maintenance of the roll component of the RSS can be understood by looking at the equation for roll vorticity forcing. Defining the streamwise vorticity of the mean flow as $\Omega = \Delta_1 \Psi$, the vorticity of the roll is estimated as the component of total streamwise

(a)



(b)

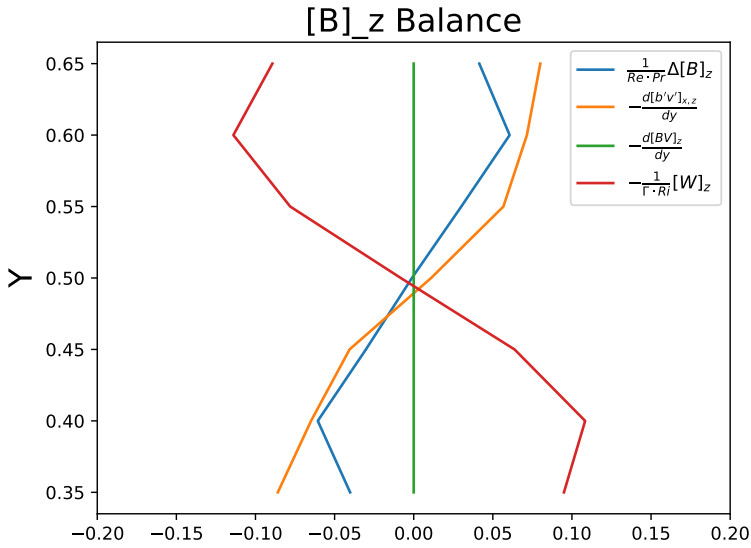


Figure 7: Fixed-point equilibrium balance among resolved fluctuation buoyancy flux divergence $\partial_y [b'v']_{x,z}$ and other terms for initially unstable state at $Ri = 0.25$ and with (a) $\epsilon = 0.02$ and (b) $\epsilon = 0.08$; $Re = 400$, $Pr = 1$.

vorticity minus its spanwise average $\Omega_r \approx \Omega - [\Omega]_z$ and its equation is:

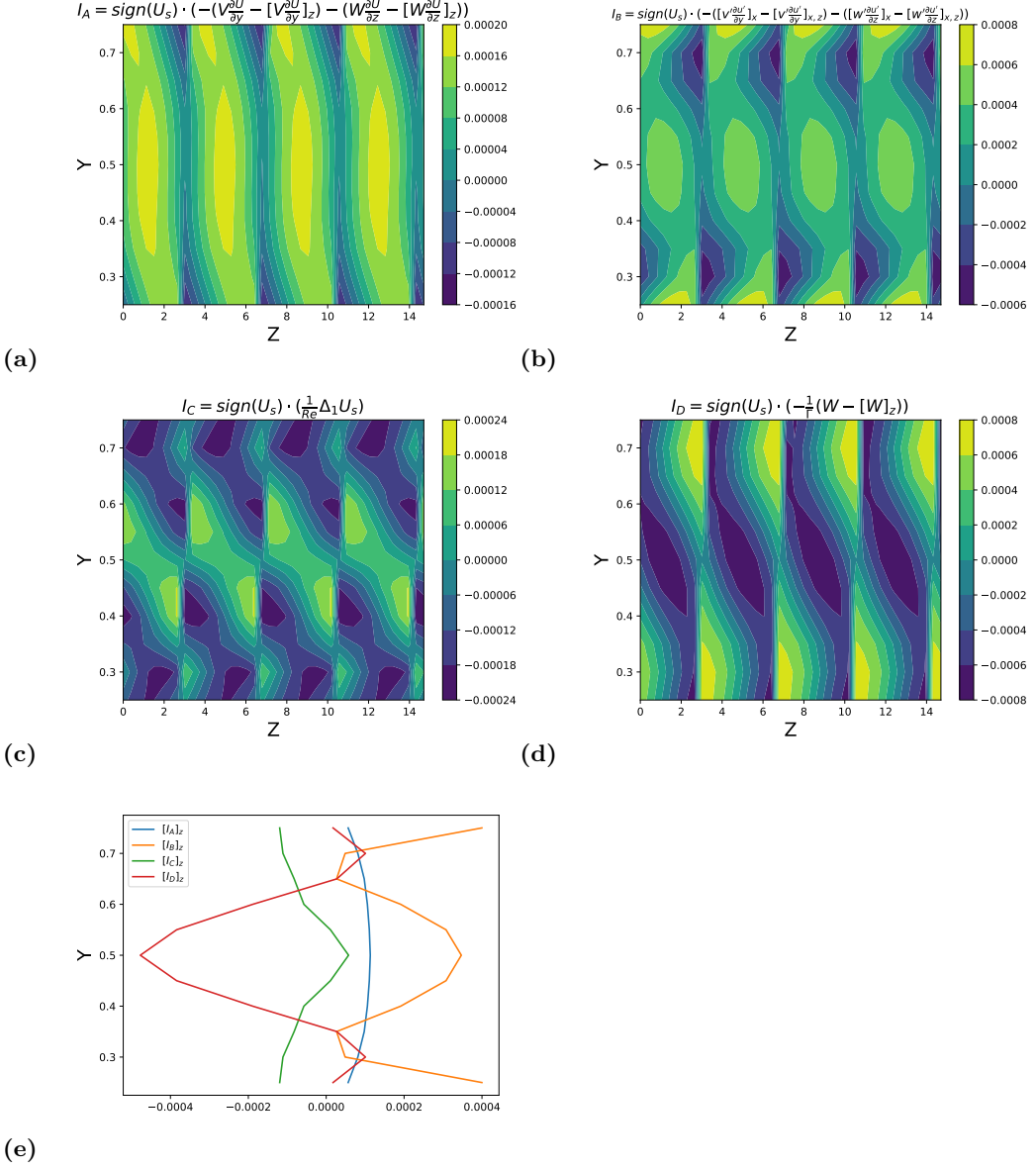


Figure 8: For the fixed-point equilibrium of an initially unstable state at $Ri = 0.25$, $Re = 400$, $Pr = 1$ and $\epsilon = 0.02$, shown is the structure of the terms maintaining the streak velocity, U_s . (a) lift up term I_A (b) Reynolds stress term I_B , (c) diffusion term I_C , (d) Coriolis term I_E . panel (e) shows spanwise average of each term.

$$\begin{aligned}
 \partial_t \Omega_r = & -((V \partial_y + W \partial_z) \Omega - [(V \partial_y + W \partial_z) \Omega]_z) + (\partial_{zz} - \partial_{yy})([v'w']_x - [v'w']_{x,z}) \\
 & - \partial_{yz}([w'w']_x - [v'v']_x) + \Delta_1 \frac{\Omega_r}{Re} + \frac{\partial_y U_s}{\Gamma} - Ri \frac{\partial(B - [B]_z)}{\partial z}
 \end{aligned} \tag{5.18}$$

Defining

$$I_E = \text{sign}(\Omega_r) \cdot (-(V\partial_y + W\partial_z)\Omega + [V\partial_y + W\partial_z]\Omega)_z \quad (5.19)$$

$$I_F = \text{sign}(\Omega_r) \cdot (\partial_{zz} - \partial_{yy})([v'w']_x - [v'w']_{x,z}) - \partial_{yz}([w'w']_x - [v'v']_x) \quad (5.20)$$

$$I_G = \text{sign}(\Omega_r) \cdot \Delta_1 \frac{\Omega_r}{Re} \quad (5.21)$$

$$I_H = \text{sign}(\Omega_r) \cdot (-Ri \frac{\partial(B - [B]_z)}{\partial z}) \quad (5.22)$$

$$I_I = \text{sign}(\Omega_r) \cdot \frac{\partial_y U_s}{\Gamma} \quad (5.23)$$

The terms I_E, I_F, I_G, I_H, I_I are the contributions from mean advection, Reynold stress divergence, diffusion, buoyancy and tilting of planetary vorticity respectively. The structure of these terms for the fixed-point equilibrium RSS initiated at $Ri = 0.25$ and with $\epsilon = 0.02$ is shown in figure 9. Panel f of this figure summarizes the contribution of each of these terms to the roll maintenance revealing that the turbulent Reynolds stresses provide the sole forcing for the fixed-point roll vorticity.

While there is some modification of the terms in the force balance for RSS maintenance in the Eady front model compared to that in wall-bounded shear flow due to the presence of Coriolis force, these balance equations are similar to those obtained in the study of wall-bounded flows (Farrell *et al.* 2016). In both the Eady front model and in wall-bounded shear flows Reynolds stresses maintain the roll against dissipation. However, in wall-bounded flows fluctuation Reynolds stress divergence acts to oppose streak maintenance and that energy helps maintain the fluctuation component of the turbulence, while, as we have seen, in the Eady front model, both the rolls and streaks are maintained by fluctuation Reynolds stresses arising from sources external to the RSS dynamics.

While previous studies (Bachman *et al.* 2017) predicted that SI adjusts the front to $Ri = 1$, our results predict that in the presence of turbulence the adjustment is to an equilibrium with $Ri_g > 1$, consistent with the predictions of our analytic lift-up matrix model from part 1 of the paper (Kim & Farrell 2025)

While the S3T SSD Eady front model supports fixed point equilibria, it also supports time-dependent equilibria in the form of limit cycles and chaotic attractors. Shown in figure 1 are equilibrium regimes identified in the parameter space of Ri and ϵ at $Re = 400$, $Pr = 1$, $r_s = 0.025$. In the next subsection, we turn our attention to time-dependent SSD equilibria.

6. Time dependent SSD equilibria

While fixed-point equilibria are maintained over a region of ϵ, Ri values and also ϵ, r_s at fixed Ri , outside this region time-dependent and turbulent states exist as seen in figure 1. Shown in figure 15 are time-dependent equilibrium diagnostics using streak energy $E_s = \frac{1}{2}[U_s^2]_{y,z}$ and $TKE = \frac{1}{2}[u'^2 + v'^2 + w'^2]_{x,y,z}$.

A limit cycle is supported by $\epsilon = 2.5$. When ϵ is increased to 6.5, quasi-periodic behavior is exhibited. When ϵ is further increased to 20, a fully turbulent solution is obtained. These

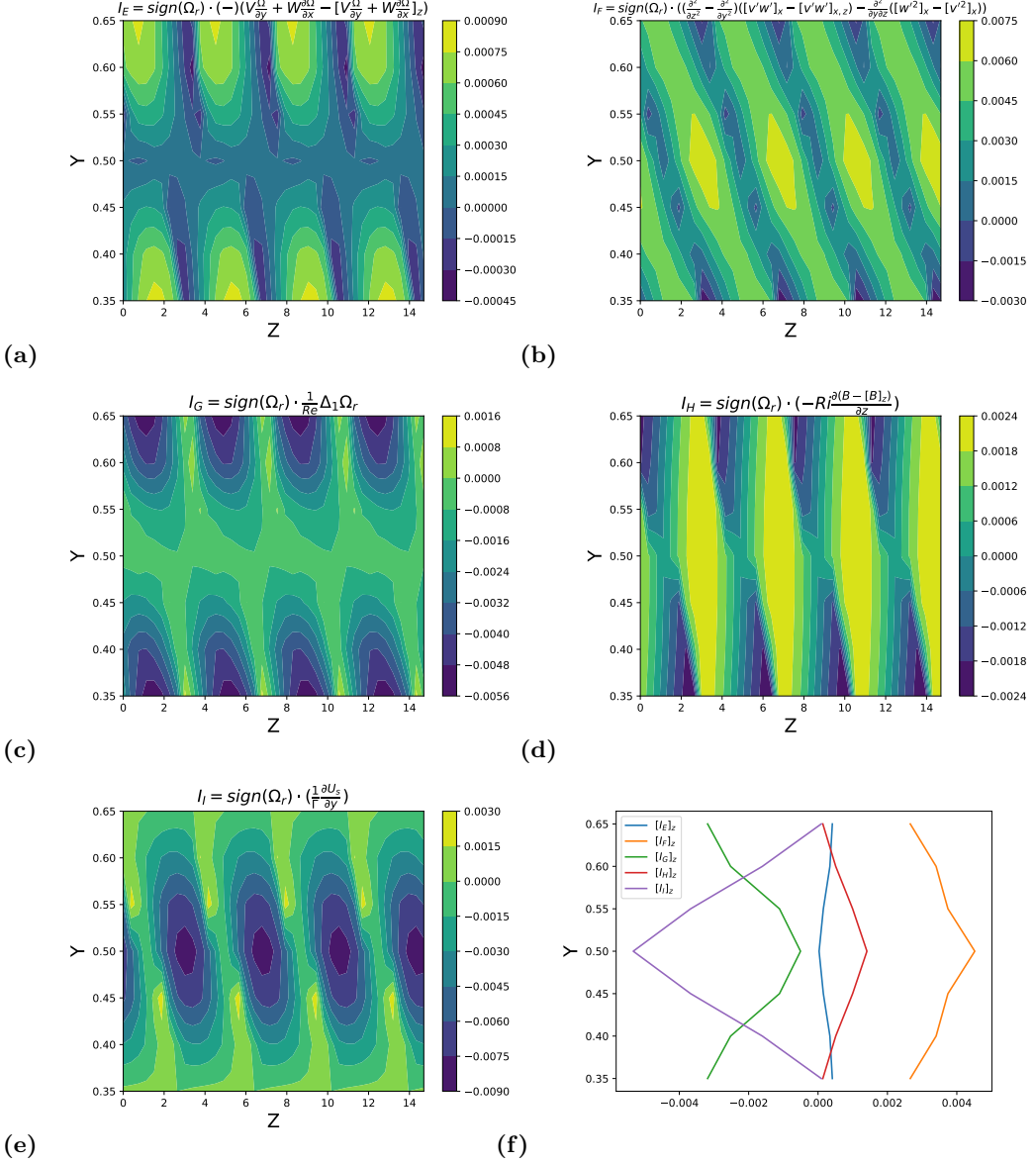


Figure 9: For the fixed-point equilibrium of an initially unstable state at $Ri = 0.25$, $Re = 400$, $Pr = 1$ and $\epsilon = 0.02$, shown is the structure of the terms maintaining the streamwise roll vorticity, Ω_r . (a) mean advection term I_E (b) Reynolds stress divergence term I_F , (c) diffusion term I_G , (d) buoyancy term I_H . (e) tilting of planetary vorticity term I_I . panel (f) shows spanwise average of each term.

time-dependent equilibrium states are similar to those previously found in wall-bounded shear flow turbulence (Farrell & Ioannou 2012; Farrell *et al.* 2016)

Time dependence of the RSS observed in figure 10 arises primarily from self-advection by the rolls and when time averages are taken the mechanism of RSS maintenance remains similar to that of fixed-point solutions discussed in section 5.3 above. Shown in figure 11

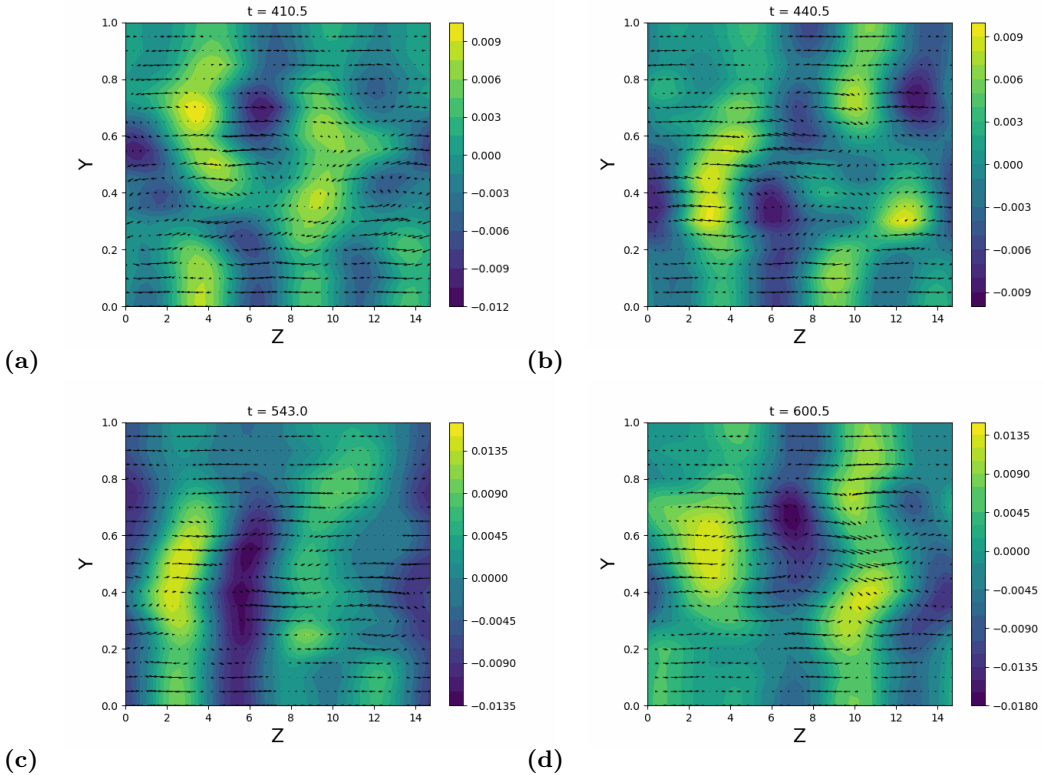


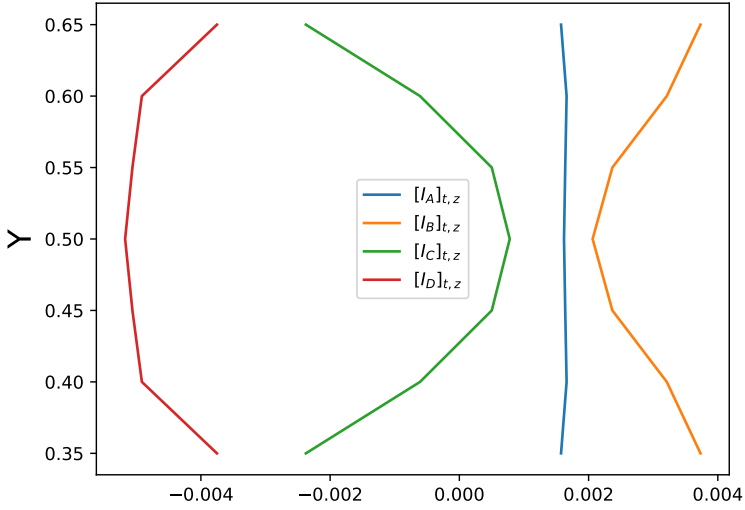
Figure 10: Snapshots of the RSS structure showing turbulent state for initial $Ri = 2$ and $\epsilon = 45$.

are the lift-up component of streak forcing, $[I_A]_{t,z}$, and $[I_A]_{y,z}$ as a function of y and t , the Reynolds stress component $[I_B]_{t,z}$, $[I_B]_{y,z}$, the damping component $[I_C]_{t,z}$, $[I_C]_{y,z}$, and the Coriolis component, $[I_D]_{t,z}$, and $[I_D]_{y,z}$ are similarly shown.

As previously found for fixed-point RSS equilibria, maintenance of the streak in the time-dependent state is due to the Reynolds stress divergence term, I_B , and the lift-up term, I_A , primarily opposed by diffusion, I_C , as shown in figure 11. As also remarked previously in discussing fixed point streak maintenance, this streak maintenance mechanism differs from that in wall-bounded shear flow. In wall-bounded shear flow streaks are maintained by lift-up while being opposed by the Reynolds stresses (Farrell *et al.* 2016). Unlike in wall-bounded shear flows, in the Eady front model there is a Coriolis term redistributing energy between the streak, U_s , and roll, $W - [W]_z$, this Coriolis coupling term, $\frac{W - [W]_z}{F}$, causes the streak U_s to lose energy when lift-up, I_A , and Coriolis coupling, I_D are combined. Therefore, maintaining the streak requires the Reynolds stress divergence term I_B .

Maintenance of the roll by vorticity forcing can be examined in a manner similar to maintenance of the streak. Unlike in the fixed point equilibrium state in which streamwise vorticity was substantially opposed by Coriolis tilting term I_I and diffusion, I_G , as shown in figure 9; in time-dependent RSS Reynolds stress vorticity forcing provides essentially all of the roll vorticity forcing and this forcing is opposed almost solely by diffusive damping as shown in figure 12

(a)



(b)

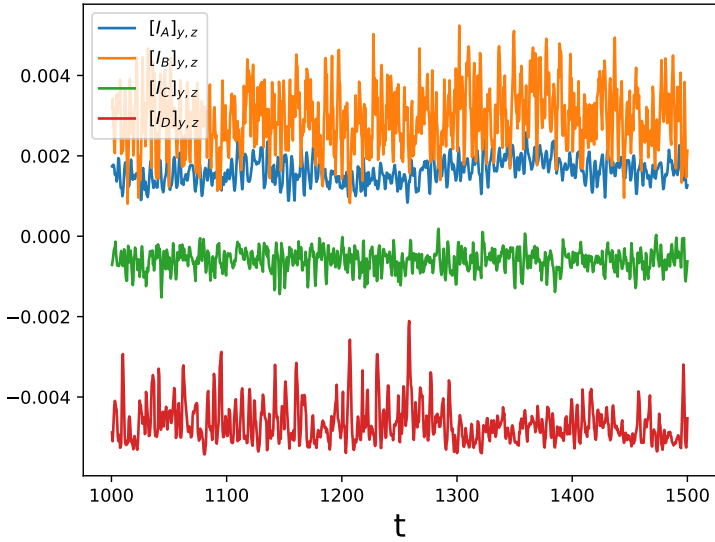
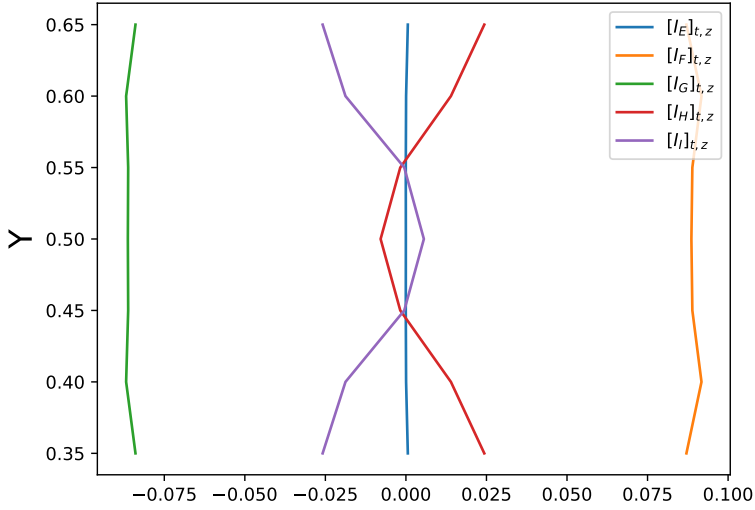


Figure 11: Equilibrium balance in time-dependent RSS turbulence. Shown are the lift-up term, $I_A(y, z, t)$, Reynolds stress term, $I_B(y, z, t)$, diffusion term, $I_C(y, z, t)$, and Coriolis term, $I_D(y, z, t)$, for initial $Ri = 2$ and $\epsilon = 45$. (a) Spanwise and time averaged; (b) averaged in the wall-normal direction y and spanwise direction z . Results are for $Re = 400$, $Pr = 1$, and $r_s = 0.025$.

(a)



(b)

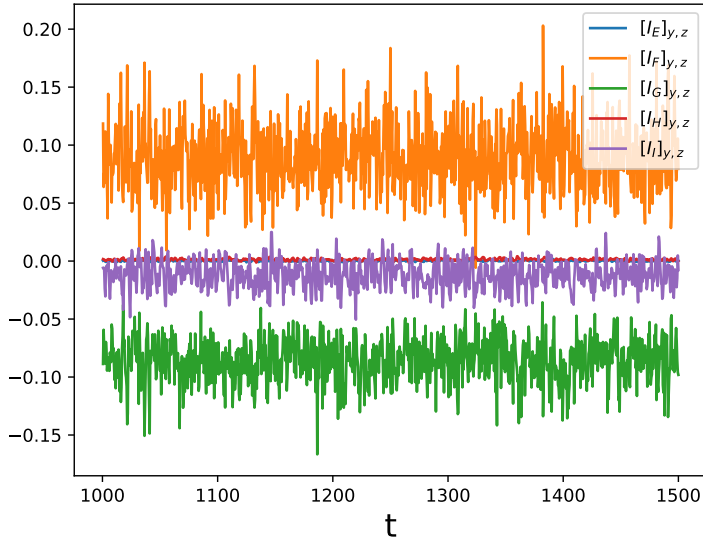
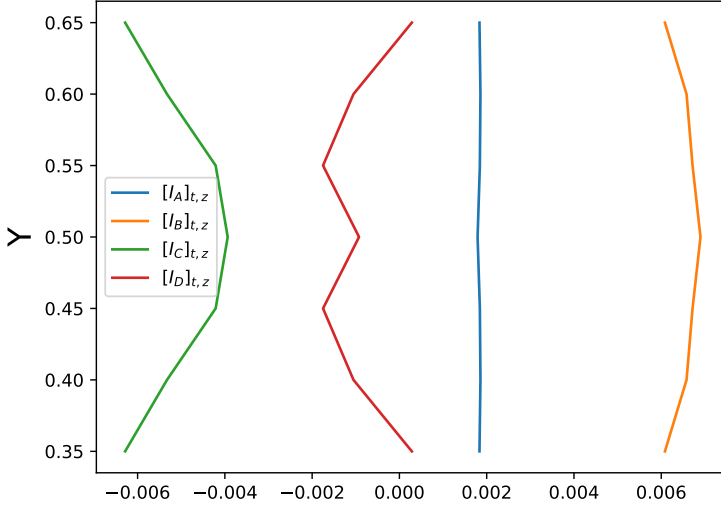


Figure 12: Equilibrium balance in time-dependent RSS turbulence. Shown are the mean advection term, $I_E(y, z, t)$, Reynolds stress divergence term, $I_F(y, z, t)$, diffusion term, $I_G(y, z, t)$, buoyancy term, $I_H(y, z, t)$, and tilting of planetary vorticity term, $I_I(y, z, t)$, for initial $Ri = 2$ and $\epsilon = 45$. (a) Spanwise and time averaged; (b) averaged in the wall-normal direction y and spanwise direction z . Results are for $Re = 400$, $Pr = 1$, and $r_s = 0.025$.

(a)



(b)

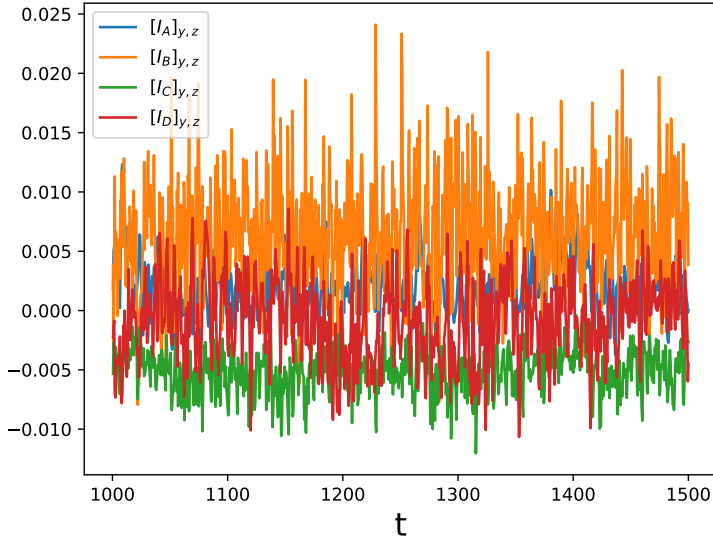
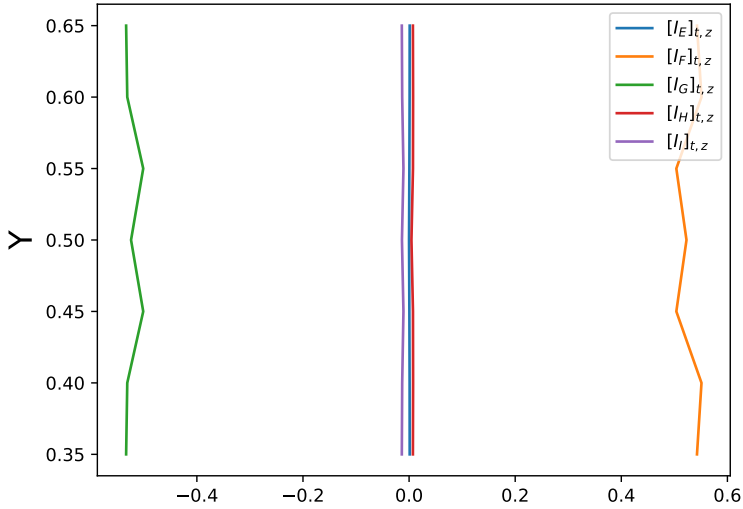


Figure 13: Equilibrium balance in time-dependent RSS turbulence. Shown are the lift-up term, $I_A(y, z, t)$, Reynolds stress term, $I_B(y, z, t)$, diffusion term, $I_C(y, z, t)$, and Coriolis term, $I_D(y, z, t)$, for initial $Ri = 0.25$ and $\epsilon = 20$. (a) Spanwise and time averaged; (b) averaged in the wall-normal direction y and spanwise direction z . Results are for $Re = 400$, $Pr = 1$, and $r_s = 0.025$.

(a)



(b)

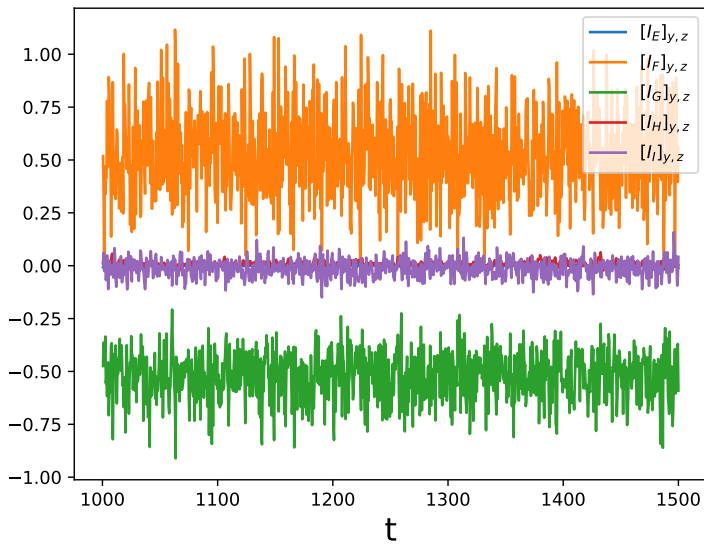
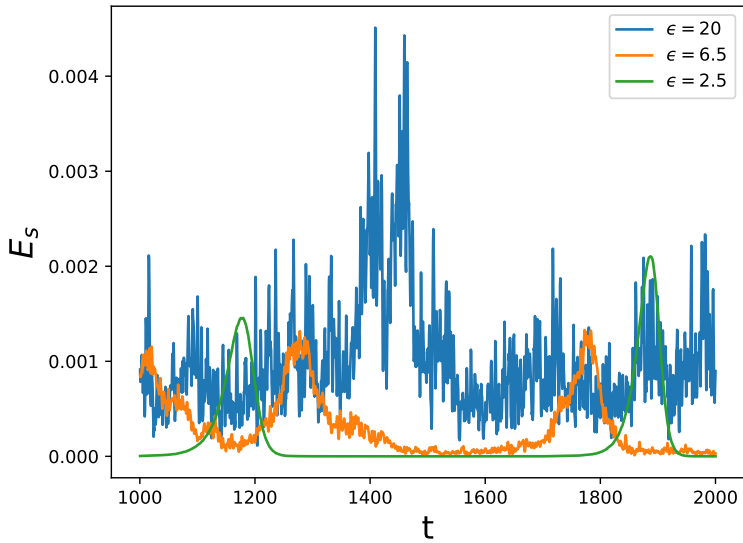


Figure 14: Equilibrium balance in time-dependent RSS turbulence. Shown are the mean advection term, $I_E(y, z, t)$, Reynolds stress divergence term, $I_F(y, z, t)$, diffusion term, $I_G(y, z, t)$, buoyancy term, $I_H(y, z, t)$, and tilting of planetary vorticity term, $I_I(y, z, t)$, for initial $Ri = 0.25$ and $\epsilon = 20$. (a) Spanwise and time averaged; (b) averaged in the wall-normal direction y and spanwise direction z . Results are for $Re = 400$, $Pr = 1$, and $r_s = 0.025$.

(a)



(b)

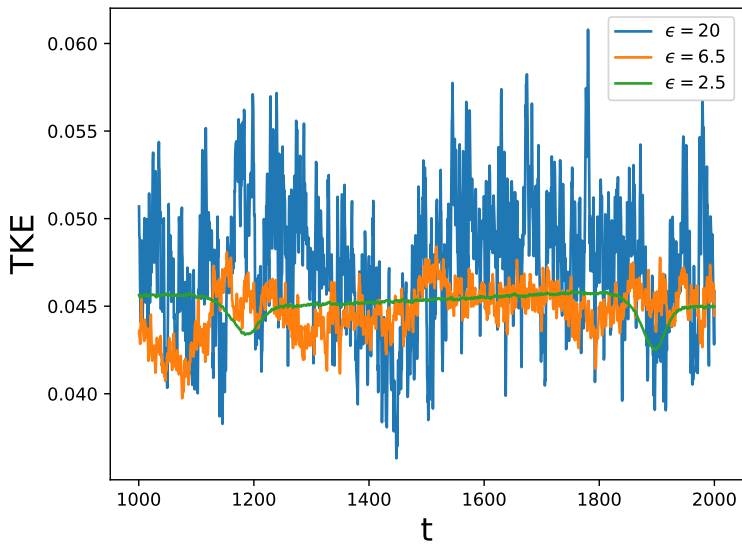


Figure 15: Time-dependent equilibrium diagnostics showing that $\epsilon = 2.5$ supports an equilibrium in the form of a limit cycle, $\epsilon = 6.5$ supports quasi-periodic behavior, and $\epsilon = 20$ supports a turbulent equilibrium. Shown are (a) streak energy, E_s , and (b) TKE. Initial $Ri = 0.25$, $Re = 400$, and $Pr = 1$.

In the next section, we turn our attention to time-dependent SSD dynamics in which modal instabilities have been suppressed.

7. SSD dynamics with modal instabilities suppressed

In part 1, we studied SSD instability of the RSS with modal instabilities (SI, baroclinic and mixed modes) suppressed. We verified that the RS torque mechanism produces RSS SSD instability in the absence of these modal instabilities. Here, we study equilibration in SSD dynamics of Eady front turbulence with modal instabilities suppressed. Studying equilibration of fronts without the support of these instabilities addresses the question of whether these instabilities are fundamentally related to the equilibration process. Recent studies of wall-turbulence equilibration and maintenance have used a similar approach (Lozano-Duran *et al.* 2016, 2020; Farrell *et al.* 2018).

The S3T SSD equations with modal instability suppressed can be written as:

$$(\Xi)_t = [G(\Xi, \lambda < 0)] + \sum_k L_{RS} C_k \quad (7.1)$$

$$(C_k)_t = A_{ke}(\lambda < 0)C_k + C_k A_{ke}(\lambda < 0)^\dagger + \epsilon \tilde{Q} \quad (7.2)$$

in which $\lambda < 0$ indicates that eigenvalues with real part greater than zero have been modified to have zero real part at each step of the integration. Compared to S3T SSD with all modal instabilities supported this system requires greater ϵ to maintain an equilibrium RSS state. This is consistent with the results from part 1 in which it was shown that SI synergistically interacts with the RS torque mechanism to support the RSS. Our study was carried out at $Ri = 0.25$, for which SI is highly unstable.

A regime diagram with parameter ϵ is shown in figure 16. This regime diagram shows that all nontrivial equilibrium regimes supported in the presence of SI continue to be supported when all modal instabilities, including SI, have been suppressed. The difference in ϵ value needed to support these equilibrium regimes implies a difference in RMS velocity of background turbulence of order two percent. For example, when SI is not suppressed, fixed-point RSS equilibria transition to time-dependent equilibria when $\epsilon_{c1} \geq 1.8$. In comparison, with modal instability suppressed, fixed-point RSS equilibria transition to time-dependent equilibria when $\epsilon_{c1\lambda < 0} \geq 8.1$. Recalling that our normalization of Q results in one unit increase of ϵ corresponding to an increase in TKE by one percent of the kinetic energy contained in the Eady front profile, it follows that the difference between the ϵ for transition to time-dependence with and without modal instability is $\epsilon_{c1\lambda < 0} - \epsilon_{c1} = 8.1 - 1.8 = 6.3$, which translates to a volume averaged RMS perturbation velocity difference $\sqrt{6.3} \cdot 0.01 \approx 0.025$ or 2.5% of the maximum velocity of the Eady model profile. Similarly, the ϵ at which transition from time-dependent to turbulent state takes place when modal instability is supported is $\epsilon_{c2} = 11.1$, while when modal instability is suppressed, it is $\epsilon_{c2\lambda < 0} = 14.8$. The difference $\epsilon_{c2\lambda < 0} - \epsilon_{c2} = 14.8 - 11.1 = 3.7$ implies a change in the RMS perturbation velocity $\sqrt{3.7} \cdot 0.01 \approx 0.019$ or 1.9% of the maximum velocity of Eady model profile. We conclude that the RS torque mechanism supports the equilibrium regimes without modal instability, requiring only small increases in volume averaged RMS perturbation velocity.

Given that observations show background turbulence levels are high in the mixed layer even when Richardson number is large (Ostrovksy *et al.* 2024), the presence of modal

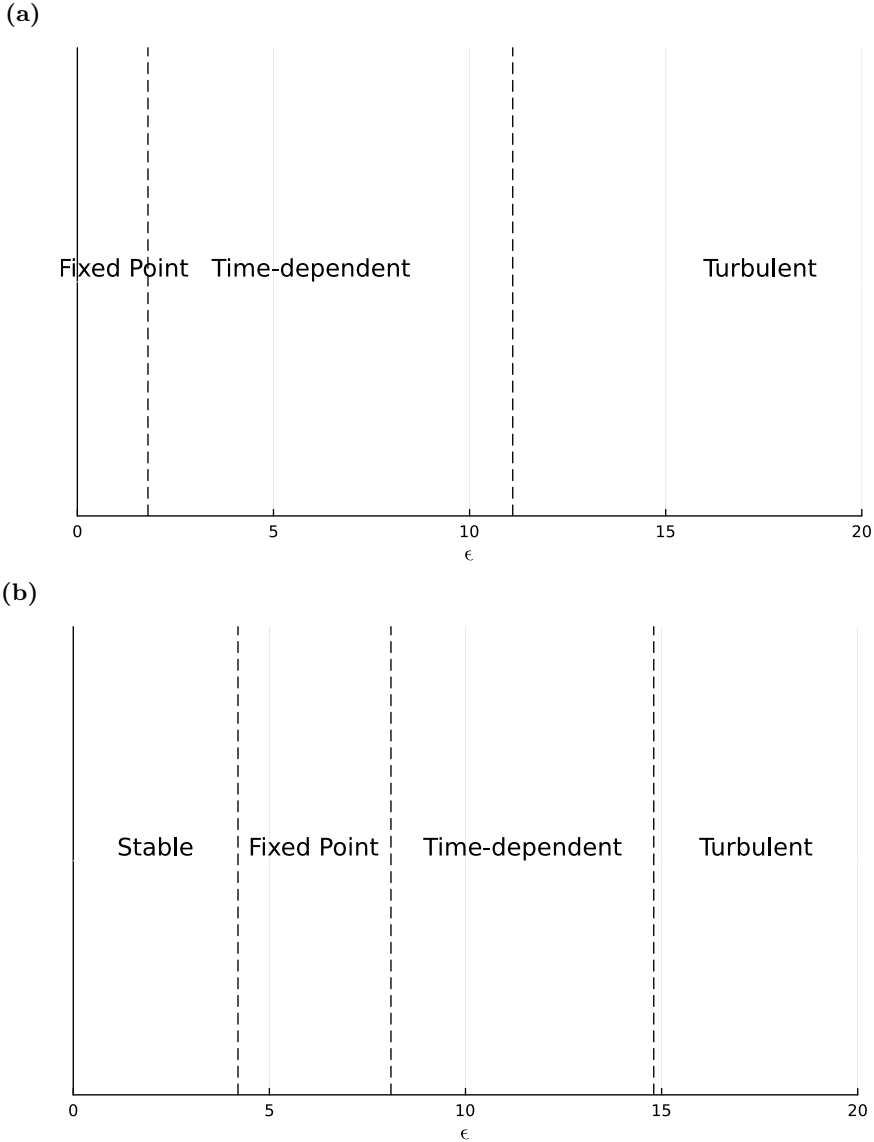
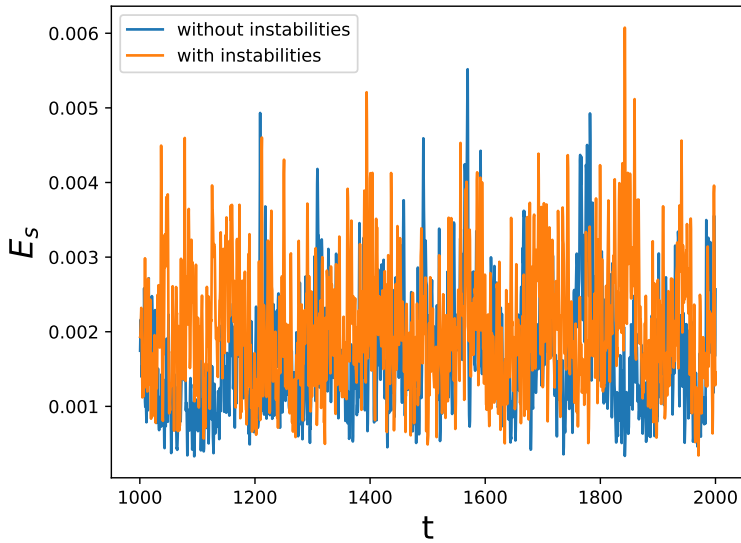


Figure 16: Equilibrium regime diagram as a function of ϵ (a) without suppression of modal instability (b) with suppression of modal instabilities (including SI) for initial $Ri = 0.25$, $Re = 400$, $Pr = 1$

instabilities, including SI, may not be as important as differences in equivalent ϵ value in supporting equilibrium RSS regimes.

RSS formation can occur solely due to the RS torque mechanism and as seen in the TKE and streak energy E_s of turbulence in figure 17, the turbulence maintained is similar whether or not instabilities are suppressed. As expected, eliminating instability growth does result in some reduction in E_s and TKE . This result is similar that in (Lozano-Duran *et al.* 2016, 2020)

(a)



(b)

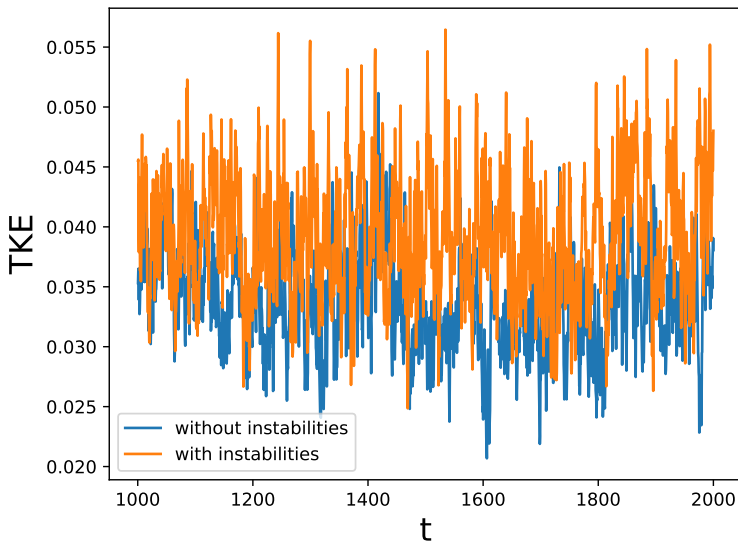


Figure 17: Maintenance of turbulent equilibria with and without modal instabilities suppressed. Shown are: (a) streak energy, E_s , and (b) TKE; for initial $Ri = 0.25$, $\epsilon = 25$, $Re = 400$, and $Pr = 1$.

8. Discussion and Conclusions

In this paper we have focused on the dynamics of turbulent front equilibration in the S3T SSD Eady model. While the traditional approach of using perturbation methods to study SI in this model provides an explanation for RSS formation, it does not provide a

comprehensive explanation for RSS formation or for RSS equilibration and, by extension, for frontal equilibration. The reason is that SI theory does not systematically account for the essential role of resolvable turbulent fluctuations in the instability and equilibration process. A comprehensive theory results when the resolvable fluctuation effects are incorporated by using a SSD formulation of the Eady front model. In part 1 of this paper we showed that linearly perturbing the SSD of the Eady front model uncovered a manifold of nonlinear instabilities that are essential to constructing a comprehensive theory of frontal dynamics. Obtaining this manifold of nonlinear instabilities was accomplished by linearly perturbing the SSD; including the second cumulant, which is a nonlinear variable, to obtain these nonlinear instabilities in the form of linear modes in a nonlinear variable. With the inclusion of these nonlinear instabilities, the initial formation of the RSS in the Eady front model was understood comprehensively as a synergistic interaction between the traditionally recognized SI manifold and this new manifold of RS destabilized modes. In the present work we exploit the fact that the Eady front model SSD is a nonlinear model for frontal dynamics to extend the perturbation results for RSS formation obtained in Part 1 to a comprehensive theory for the dynamics of RSS equilibration and by extension frontal equilibration. In parameter space (Ri, ϵ) , we found fixed point, time-dependent, and turbulent equilibria. These analytic equilibria have no counterpart in traditional SI theory. By analyzing balance equations for streak amplitude, U_s , and roll vorticity, Ω_x , we determined the physical mechanism underlying these equilibria. The results show that the streak, U_s , in both fixed point and time-dependent RSS states is maintained by Reynolds stress divergence, I_B , augmented by lift-up, I_A , in balance with diffusion, I_C , augmented by Coriolis force, I_D . It is of interest to compare this RSS streak balance with that in wall-bounded shear flow turbulence, where the RSS is maintained in dominant balance between acceleration by lift-up and deceleration by Reynolds stress divergence. The reason for this difference is fundamentally due to the fluctuations in fully developed wall-turbulence being maintained by extracting energy from the streak, requiring a strong streak deceleration by the Reynolds stresses, while in the Eady front problem the fluctuations are being maintained by parameterized background turbulence. The level of background turbulence maintained by our parameterization, a few percent of mean TKE, is comparable to that in a carefully constructed wind tunnel and is likely to be an underestimate for the PBL.

Turning to the vorticity balance maintaining the roll circulation for fixed point and time-dependent RSS in the Eady front model, we found that this balance is similar to that in wall-bounded shear flow turbulence in which the streamwise vorticity component, Ω_x , is maintained primarily by Reynolds stress torque, I_F , balanced by diffusion, I_G , except that in the case of the Eady front model there is some augmentation of diffusive damping by a contribution from the Coriolis force.

It is remarkable that the RS mechanism establishes and maintains RSS at equilibrium as fixed-point or time-dependent states in the absence of symmetric instability, either because initial $Ri > 1$ or because instabilities have been suppressed. While fixed-point, time-dependent, and turbulent RSS states are not supported at equilibrium by SI acting alone, we find these RSS equilibria are supported when both the RS and the SI mechanism coexist.

A primary component of the equilibration mechanism is adjustment of the gradient Richardson number to exceed unity, which occurs even when symmetric instability is supported by the choice of initial Richardson number. However, as the background free stream turbulence excitation parameter, ϵ , increases the equilibrated state is adjusted to

greater $[\frac{\partial B}{\partial y}]_z$. At sufficiently high ϵ the RSS state becomes time-dependent and ultimately a turbulent self-advecting RSS state is established but the mechanism of equilibration by increasing Ri_g is maintained.

Given observations of deep transport across the mixed layer, restricted areas satisfying conditions for SI, and evidence for sufficient mixed layer TKE to support the RS mechanism of RSS formation; the manifold of nonlinear RSS instabilities and their finite amplitude equilibria identified in this study provide the basis for constructing a more comprehensive theory of turbulence structure and transport in the PBL of the ocean and atmosphere.

9. Appendix

9.1. Details of equation 3.12 – 3.16

Here are the details of the operators presented in equation 3.12 – 3.16

$$LV_{11}(V) = (k^2 V_y - V_{yzz} + k^2 V \partial_y - V_{zz} \partial_y - 2V_{yz} \partial_z - V_y \partial_{zz} - 2V_z \partial_{yz} - V \partial_{yzz}) \\ + [(ik)(V_y \partial_y + V \partial_{yy})](-ik \Delta_2^{-1} \partial_y) \quad (9.1)$$

$$+ (k^2 V_z - V_{zzz} + V_{yz} \partial_y + V_z \partial_{yy} + V_y \partial_{yz} + V \partial_{yyz} - 2V_{zz} \partial_z - V_z \partial_{zz})(-\Delta_2^{-1} \partial_{yz})$$

$$LW_{11}(W) = (k^2 W \partial_z + W_{yy} \partial_z + W_y \partial_{yz} + W_{yyz} + W_{yz} \partial_y - W_{zz} \partial_z - 2W_z \partial_{zz} - W \partial_{zzz}) \\ + (ikW_y \partial_z + ikW \partial_{yz})(-ik \Delta_2^{-1} \partial_y) \\ + (2W_{yz} \partial_z + 2W_z \partial_{yz} + W_{zz} \partial_y + W_{zz} \partial_y + W_y \partial_{zz} + W \partial_{zz})(-\Delta_2^{-1} \partial_{yz}) \quad (9.2)$$

$$LV_{12}(V) = [(ik)(V_y \partial_y + V \partial_{yy})](\Delta_2^{-1} \partial_z) \\ + (k^2 V_z - V_{zzz} + V_{yz} \partial_y + V_z \partial_{yy} + V_y \partial_{yz} + V \partial_{yyz} - 2V_{zz} \partial_z - V_z \partial_{zz})(-ik \Delta_2^{-1}) \quad (9.3)$$

$$LW_{12}(W) = (ikW_y \partial_z + ikW \partial_{yz})(\Delta_2^{-1} \partial_z) \\ + (2W_{yz} \partial_z + 2W_z \partial_{yz} + W_{zz} \partial_y + W_{zz} \partial_y + W_y \partial_{zz} + W \partial_{zz})(-ik \Delta_2^{-1}) \quad (9.4)$$

$$LV_{21}(V) = -(V_z \partial_y + V \partial_{yz})(-ik \Delta_2^{-1} \partial_y) + (ikV \partial_y)(-\Delta_2^{-1} \partial_{yz})$$

$$LW_{21}(W) = (ikW_y) - (W_z \partial_z + W \partial_{zz})(-ik \Delta_2^{-1} \partial_y) + (ik)(W_z + W \partial_z)(-\Delta_2^{-1} \partial_{yz}) \quad (9.5)$$

$$LV_{22}(V) = -(V_z \partial_y + V \partial_{yz})(\Delta_2^{-1} \partial_z) + (ikV \partial_y)(-ik \Delta_2^{-1}) \quad (9.6)$$

$$LW_{22}(W) = -(W_z \partial_z + W \partial_{zz})(\Delta_2^{-1} \partial_z) + (ik)(W_z + W \partial_z)(-ik \Delta_2^{-1}) \quad (9.7)$$

REFERENCES

- BACHMAN S.D., KEMPER B. F., TAYLOR J.R. & THOMAS L.N. 2017 Parameterization of Frontal Symmetric Instabilities. I: Theory for Resolved Fronts. *Ocean Modeling* **109** 72-95
- BOSSE A., TESTOR P., DAMIEN P., ESTOURNEL C., MARSALEIX P., MORTIER L., PRIEUR L. & TAILLANDIER V. 2022 Wind-Forced Submesoscale Symmetric Instability around Deep Convection in the Northwestern Mediterranean Sea. *Fluids* **6** 123
- BUTLER, K. M. & FARRELL, B. F. 1992 Three-dimensional optimal perturbations in viscous shear flows. *Phys. Fluids* **4**, 1637–1650.
- CONSTANTINOU, N. C., LOZANO-DURÁN, A., NIKOLAIDIS, M.-A., FARRELL, B. F., IOANNOU, P. J. & JIMÉNEZ, J. 2014b Turbulence in the highly restricted dynamics of a closure at second order: comparison with DNS. *J. Phys. Conf. Ser.* **506**, 012004.
- LOZANO-DURAN A., NIKOLAIDIS M. A., CONSTANTINOU N. C. & KARP M. 2019 Wall turbulence without modal instability of the streaks. *arXiv:1909.05490*

- LOZANO-DURAN A., CONSTANTINOU N. C., NIKOLAIDIS M. A. & KARP M. 2020 Cause-and-effect of linear mechanisms sustaining wall turbulence. *J. Fluid Mechanics* **914** A8 1-A8 58
- EADY E.T. 1949 Long Waves and Cyclone Waves. *Telius* 33-52
- EMANUEL, K. 1988 Observational Evidence of Slantwise Convective Adjustment. *Amer. Meteo. Soci* **116** 1805-1816
- FARRELL, B. F. & IOANNOU, P. J. 2012 Dynamics of streamwise rolls and streaks in turbulent wall-bounded shear flow. *J. Fluid Mech.* **708**, 149-196.
- FARRELL, B. F. & IOANNOU, P. J. 2016 Structure and mechanism in a second-order statistical state dynamics model of self-sustaining turbulence in plane Couette flow. *Phys. Rev. Fluids* (submitted, arXiv:1607.05020).
- FARRELL, B. F., IOANNOU, P. J. & M.-A., NIKOLAIDIS 2016 Instability of the roll/streak structure induced by free-stream turbulence in pre-transitional Couette flow. *Phys. Rev. Fluids* (submitted, arXiv:1607.05018).
- FARRELL B. F., IOANNOU P. J., JIMENEZ J., CONSTANTINOU N. C., LOZANO-DURAN A. & NIKOLAIDIS M. A. 2016 A statistical state dynamics-based study of the structure and mechanism of large-scale motions in plane Poiseuille flow. *J. Fluid Mechanics* **809** 290-315
- FARRELL B. F., IOANNOU P. J. & NIKOLAIDIS M. A. 2018 Parametric mechanism maintaining Couette flow turbulence is verified in DNS. *Center for Turbulence Research Proceedings of the Summer Program 2018*
- FARRELL, B. IOANNOU, P 2019 Statistical State Dynamics: A New Perspective on Turbulence in Shear Flow. *Zonal Jets Phenomenology, Genesis, and Physics. Ed. Boris Galperin and Peter L. Read. Cambridge University Press 2019.* 380-400.
- FARRELL B. F., IOANNOU P. J. & NIKOLAIDIS M. A. 2022 Mechanism of Roll-Streak Structure Formation and Maintenance in Turbulent Shear Flow. *arXiv:2205.07469*.
- FORRYAN A., MARTIN A. P., SROKOSZ M. A., POPOVA E. E., PAINTER S. C. & RENNER A. H. H. 2013 A new observationally motivated Richardson number based mixing parametrization for oceanic mesoscale flow. *J. Geophysical Research: Oceans* **118** 1405-1419
- HAINE, T. W. N. & MARSHALL J. 1997 Gravitational, Symmetric, and Baroclinic Instability of the Ocean Mixed Layer. *J. Physical Oceanography* **28** 634-658
- KIM, E. & FARRELL, B.F. 2025 Statistical State Dynamics based study of turbulence in Eady fronts. Part 1. Instability. *arXiv:2506.11993*
- MACK, S.A. & SCHOEBERLEIN H.C. 2003 Richardson Number and Ocean Mixing: Towed Chain Observations. *J. Physical Oceanography* **34** 736-754
- NIKOLAIDIS M. A., IOANNOU P. J. & FARRELL B. F. 2024 Fluctuation covariance-based study of roll-streak dynamics in Poiseuille flow turbulence. *J. Fluid Mechanics* **988** A14.
- OSTROVSKY L., SOUSTOVA I., TROITSKAYA Y. & GLADSKIKH D. 2024 Evolution of small-scale turbulence at large Richardson numbers. *Nonlin. Processes Geophys.* **31** 219-227
- PATERAS S.C. & BAKAS N.A. 2017 Transient Growth of Ageostrophic Perturbations in a Baroclinic Shear Flow. *Perspectives on Atmospheric Sciences* 377-384
- PEREZ R.C., CRONIN M.F. & KESSLER W.S. 2010 Tropical Cells and a Secondary Circulation near the Northern Front of the Equatorial Pacific Cold Tongue*. *J. Physical Oceanography* **40** 2091-2106
- SAVELYEV, I., THOMAS, L, SMITH, G.B., WANG Q., SHEARMAN, R. K., HAACK, T., CHRISTMAN A. J., BLOMQUIST B., SLETTEN M., MILLER, W.D. & FERNANDO H.J.S. 2018 Aerial Observations of Symmetric Instability at the North Wall of the Gulf Stream *Geophysical Research Letters* **45**, 236-244
- SCHMID, P. J. & HENNINGSON, D. S. 2001 *Stability and Transition in Shear Flows*. Springer, New York.
- STAMPER M & TAYLOR J 2016 The transition from symmetric to baroclinic instability in the Eady model. *Ocean Dynamics* **67**, 65-80.
- STONE, P 1966 On non-geostrophic baroclinic stability. *J. Atmospheric. Sciences.* **23**.
- STONE, P 1970 On non-geostrophic baroclinic stability: Part ii. *J. Atmospheric. Sciences.* **27**.
- STONE, P 1971 Baroclinic stability under non-hydrostatic conditions. *J. Fluid. Mech.* **45**.
- TANDON, A & GARRETT, C 1994 Mixed layer restratification due to a horizontal density gradient. *J. Phys. Oceanogr.* **24**, 1419-1424.

- TAYLOR, J & FERRARI, R 2009 On the equilibration of a symmetrically unstable front via a secondary shear instability. *J. Fluid Mech* **622**, 103-113.
- TAYLOR, J & FERRARI, R 2009 Buoyancy and Wind-Driven Convection at Mixed Layer Density Fronts. *J. Phys. Oceanogr.* **40**, 1222-1242.
- THOMAS, L. N. 2005 Destruction of Potential Vorticity by Winds. *J. Physical. Oceanography* **35** (5), 2457-2466.
- THOMAS, L. N., TAYLOR J. R., FERRARI R. & JOYCE T. M. 2013 Symmetric instability in the Gulf Stream. *Deep Sea Research Part II Topical Studies in Oceanography* **91**, 96-110.
- THOMAS, L. N., TAYLOR J. R., D'ASARO, E. A., KLYMAK, J. M. & SHCHERBINA, A. 2016 Symmetric Instability, Inertial Oscillations, and Turbulence at the Gulf Stream Front. *J. Physical Oceanography* **46**, 197-217.
- TREFETHEN, L. N. & EMBREE M. 2005 Spectra and Pseudospectra: The Behavior of Nonnormal Matrices and Operators. *Princeton University Press, Princeton*
- WIENKERS, A., THOMAS, L. & TAYLOR J. 2022a The influence of front strength on the development and equilibration of symmetric instability. Part 1. Growth and saturation. *J. Fluid Mech.* **926**.
- WIENKERS, A., THOMAS, L. & TAYLOR J. 2022b The influence of front strength on the development and equilibration of symmetric instability. Part 2. Nonlinear evolution. *J. Fluid Mech.* **926**.
- ZEMSKOVA, V , PASSAGGIA, P ,& WHITE B 2019 Transient energy growth in the ageostrophic Eady model. *J. Fluid. Mech.* **885**, 1419-1424.
- ZHOU H., DEWAR W., YANG W., LIU H., CHEN X., LI R., LIU C. & GOPALAKRISHNAN G. 2022 Observations and modeling of symmetric instability in the ocean interior in the Northwestern Equatorial Pacific. *Commun Earth Environ* **3** 28